

Self-Consistent Renormalization Model of Mott Gap Collapse in the Cuprates

R.S. Markiewicz

Physics Department, Northeastern University, Boston MA 02115, USA

A generalized antiferromagnetic approach to the Mott transition is analyzed with special emphasis on electron doped cuprates, where evidence for electronic phase separation is weak or absent. Fluctuations are incorporated via a self-consistent renormalization, thereby *deriving* a ‘nearly-antiferromagnetic Fermi liquid’ susceptibility. The calculation is sensitive to hot-spot effects. Near optimal doping, an approximately electron-hole symmetrical Mott gap collapse is found (quantum critical points). The calculation satisfies the Mermin-Wagner theorem (Néel transition at $T = 0$ only – unless interlayer coupling effects are included), and the mean-field gap and transition temperature are replaced by pseudo-gap and onset temperature. The resulting susceptibility is used to calculate the doping dependence of the photoemission dispersion, in excellent agreement with experiment. Discussions of interlayer coupling, doping dependence of U , and extension to a three-band model are included.

I. INTRODUCTION

Schrieffer, Wen, and Zhang¹ originally proposed that the magnetic insulating phase in underdoped cuprates could be understood via a spin density wave (SDW) approach to the Mott transition, and successfully described the spin wave spectrum of the undoped parent compound, which is an antiferromagnetic (AFM) insulator. Kampf and Schrieffer² showed that precursors of the Mott transition could give rise to a *pseudogap* in the quasiparticle spectrum, between incipient upper and lower Hubbard bands (U/LHBs). Attempts were quickly made to go beyond mean field theories by incorporating fluctuation effects, but a number of problems soon arose. While some calculations found evidence for pseudogaps³, others did not⁴. Many calculations found evidence for instabilities – either to incommensurate magnetism⁵ or to phase separation⁶.

In a broader context, there is an ongoing controversy as to whether the Mott transition can be described starting from a band structure picture, or whether the strong correlations require a local point of view. For large hole dopings, a local picture seems justified by the observation that the magnetic correlation length ξ remains finite in the presence of the pseudogap, whereas mode coupling theories would predict a divergence in ξ as temperature $T \rightarrow 0$. However, this effect may be due to nanoscale phase separation physics.

Newer experiments have suggested that indeed phase separation and/or stripe physics is present in the hole doped cuprates^{7,8} down to arbitrarily small dopings⁹, thereby validating the early models. It remains difficult

to develop a theory which simultaneously treats both the effects of strong fluctuations and (nanoscale) phase separation. A simpler alternative has recently been proposed. While phase separation is a significant complication for *hole doping*, this instability is greatly reduced or absent in *electron-doped* materials^{10,11}, allowing a much simpler analysis. Moreover, for electron doping, the band picture involving short-range AFM order seems justified, in that the correlation length diverges for all dopings up to the QPT.

Remarkably, simple mean field calculations suggest an explanation for both the electron-hole asymmetry¹² and the anomalous properties of the electron-doped cuprates^{11,13}. Thus, for a band structure with electron-hole symmetry, the AFM state is stable only at half filling, being unstable against phase separation (negative compressibility) for any finite doping (this is also found in dynamic mean field theory¹⁴). Introducing electron-hole asymmetry (here via a finite second-neighbor hopping t'), the doped system remains unstable for any finite doping *toward* the Van Hove singularity (VHS) (hole-doping for $t' < 0$). However, for doping *away* from the VHS, electronic phase separation can be eliminated if the asymmetry is large enough. Similarly, the RPA spin wave spectra¹ are found to be stable in electron doped materials, even when both upper and lower Hubbard bands cross the Fermi level¹³, while they are unstable against incommensurate SDWs in the presence of hole doping^{15,16}.

The resulting physics is much simpler for electron doping, with the gap decreasing gradually as the UHB fills. A quantum critical point (QCP) (Mott gap closing) is found¹⁰ just beyond optimal doping, which can be understood theoretically¹¹ if the effective Hubbard U parameter decreases with doping (e.g., due to screening). Since the pseudogap is associated with short-range AFM order, it appears predominantly at the hot spots – the points where the Fermi surface crosses the Brillouin zone boundary for long-range AFM order. As the gap shrinks, both upper and lower Hubbard bands cross the Fermi level, leading to two-band conduction, as observed experimentally¹⁷.

The pseudogap closing also leads to a QCP near optimal doping in hole doped cuprates, consistent with predictions^{18,19}. However, its possible observation²¹ is complicated by the presence of stripes, and this QCP has been analyzed in terms of a mode-coupling theory of two dimensional CDWs, taken as a model for stripes^{22,23}. Remarkably, for *both* electron and hole doping, the QCP occurs close to the point where hot spots vanish. It will be shown why this is expected to be the case²⁰.

Thus, there appear to be *alternative pathways to Mott gap collapse* in the cuprates. Since the transition is better behaved in electron-doped cuprates, it makes sense to develop a model which can describe the transition for these materials, then use the acquired insights to tackle the harder problem of hole doping with the attendant (nanoscale) phase separation. Here the mean field and RPA results are extended by incorporating fluctuations via mode-coupling theory²⁴, following Moriya's self-consistent renormalization (SCR)^{25,26} procedure. Mode coupling theories have been applied to charge density wave (CDW) systems^{27,22}, and have led to a successful theory of weak itinerant magnetic systems^{25,26}. They have also been used to study glass transitions²⁸, and recently extended to glasses in cuprates²³. The mode coupling analysis is particularly convenient, being the simplest model for which the Mermin-Wagner theorem is satisfied, and one can try to understand how to have a Mott (pseudo)gap without a superlattice. The present calculations are in general consistent with the results of Ref 3. The resulting pseudogaps compare well with recent photoemission experiments, while parallel results for hole doping provide clear evidence for additional complications associated with stripe phases.

The SCR theory involves a set of parameters²⁹ which also arise in the nearly antiferromagnetic Fermi liquid (NAFL)³⁰ and spin fermion^{31,32} models and in renormalization group (RG) calculations of quantum phase transitions^{33,34}. These parameters are generally estimated empirically from experiments. However, the good agreement between experiment and mean field theory for electron doped cuprates encourages us to try to *calculate* these parameters from first principles, in terms of a renormalized Hubbard parameter U_{eff} and a mode coupling parameter u . Most of the defining integrals are dominated by the region of hot spots.

Some of these results have been reported previously in the discussion of the mean-field results^{11,20} and in a conference proceedings³⁵. This paper is organized as follows. Section II presents an outline of the calculation, including the reduction to one band (Appendix A), doping dependence of U (Appendix B), and path integral formalism (Appendix C). The fluctuation-induced correction to the susceptibilities is calculated, and is found to diverge for a two-dimensional system, driving the Néel temperature T_N to zero (Mermin-Wagner theorem). Since the transition occurs when a Stoner factor equals unity, it is controlled by the *real* part of the bare susceptibility. Hence Section III reviews the properties of $Re\chi$, showing that plateaus in χ as a function of doping, \vec{q} , or ω are all controlled by the physics of hot spots. In turn, these plateaus provide *natural phase boundaries* for QCPs²⁰. The resulting susceptibility has a form similar to that postulated for a nearly antiferromagnetic Fermi liquid (NAFL), and a calculation of the NAFL parameters (Appendix D) finds that there are *extra* (cutoff) parameters, which cannot be neglected. In Section IV, this renormalized susceptibility is incorporated into the lowest-order correction to the

electronic self energy, allowing a calculation of the spectral function associated with the *pseudogap* ($T_N = 0$). Excellent agreement is found with the ARPES spectra of NCCO. Section V shows that inclusion of interlayer hopping leads to a finite T_N (Appendix E). Results are discussed in Section VI, and Conclusions in Section VII.

II. OUTLINE OF THE CALCULATION

A. $t - J$ vs Mode-Coupling $t - U$ Models

While the strongly correlated Hubbard model is often approximated by a $t - J$ model, this is not appropriate in the present analysis. In the electron doped cuprates, both Hubbard bands need to be accounted for, since (a) ARPES can detect both bands (at least up to the Fermi level), and (b) the Mott gap is found to collapse with doping, leading to an overlapping of both bands with the Fermi level. This situation is difficult to incorporate into the $t - J$ model, where one Hubbard band is neglected. For this reason, an alternative procedure is used in the present paper.

While mean field calculations reproduce the low temperature properties, they do not account for thermal fluctuations, and hence predict that Neel order persists to too high temperatures – indeed, for a two-dimensional system, Neel order can exist only at $T = 0$ (Mermin-Wagner theorem)³⁶. Even when fluctuation effects depress the onset of *long-range order*, *short-range order* can still persist up to the mean-field transition temperature, producing a pseudogap similar to the ones found in one-dimensional CDWs²⁷. In the AFM these fluctuations are associated with spin wave excitations, in particular the Goldstone modes near \vec{Q} . Here, this effect is calculated, following the self consistent renormalization (SCR) scheme of Moriya^{25,26}.

The calculation recovers the mean-field results, that antiferromagnetism is stable for electron doping (in the presence of a second-neighbor hopping parameter $t' < 0$), but for hole doping the lowest energy state is either an incommensurate SDW³⁷ or phase separated^{38,39}. [Unrestricted Hartree-Fock calculations find that for $t' = 0$, the incommensurate antiferromagnetic state has lower free energy, while for sufficiently negative t' , the phase separated state is the lower free energy state⁴⁰.] While the SCR technique can be generalized to deal with competing phases⁴¹, only the antiferromagnetic fluctuations will be treated here. To keep the results consistent with a low-doping $t - J$ analysis, the mode coupling parameter is chosen to reproduce the $t - J$ expression for the spin stiffness parameter at half filling.

B. Model Dispersion and Doping Dependence of U

The cuprates are treated in a one-band model. By comparison with a 3-band model (Appendix A), this can be shown to be an excellent approximation for the magnetic properties. The bare electronic dispersion is

$$\epsilon_k = -2t(c_x + c_y) - 4t'c_xc_y, \quad (1)$$

with $c_i = \cos k_i a$. The dispersions for undoped $\text{Sr}_2\text{CuO}_2\text{Cl}_2$ SCOC and electron-doped NCCO can be fit by assuming $t = 0.326\text{eV}$, $t'/t = -0.276$, with U taken as an effective doping dependent parameter¹¹, with $U = 6t$ at half filling. Remarkable, virtually the same parameters are found⁴² to describe the spin wave spectrum⁴³ in La_2CuO_4 : $t = 0.34\text{eV}$, $t'/t = -0.25$, and $U/t = 6.2$. The former values will be used here.

Many textbooks on strong correlation physics^{44,45} note that the Hubbard U should be doping dependent, based on the original results of Kanamori⁴⁶, but there are no satisfactory results for the doping dependence in the cuprates. A simple model calculation, which gives semi-quantitative agreement with experiment in NCCO^{10,11}, is described in Appendix B.

C. Mode Coupling Calculation: Derivation of NAFL Parameters

A naive perturbation theory breaks down due to mode coupling, and the SCR scheme is introduced to calculate the renormalized susceptibility near the antiferromagnetic wave vector \vec{Q} . The (path integral) formalism is reviewed in Appendix C, and only the main results are given here. The divergence of the susceptibility is controlled by the (inverse) Stoner factor $\delta_q = 1 - U\chi_0(\vec{Q} + \vec{q}, \omega)$, where χ_0 is the bare magnetic susceptibility. Within the SCR, δ_0 is renormalized to $\delta > 0$, so there is no divergence, but when $\delta = 0^+$ there are strong fluctuations (pseudogap regime). The physics is controlled by the dispersion of δ near \vec{Q} ,

$$\delta_q(\omega) = \delta + Aq^2 + A_zq_z^2 - B\omega^2 - iC\omega, \quad (2)$$

Eq. C18; the important parameters A , B , and C are evaluated in Appendix D (B is small and can generally be ignored). This leads to a susceptibility

$$\chi(\vec{q}, \omega) = \frac{\chi_Q}{1 + \xi^2[(\vec{q} - \vec{Q})^2 + a_z(q_z - Q_z)^2] - \omega^2/\Delta^2 - i\omega/\omega_{sf}}, \quad (3)$$

with coefficients given by Eqs. C39-C42 in terms of A , B , and C . Here and below \vec{q} and \vec{Q} are treated as two-dimensional vectors, while q_z is introduced explicitly, and $a_z = A_z/A$. Interlayer coupling will be ignored, $a_z = 0$, until Section V and Appendix E, where it is considered

as a possible mechanism for generating a finite Néel temperature. The similarity of Eq. 3 to the corresponding result for CDW's²² should be noted – the SCR is a form of mode coupling theory.

Equation 3 is of nearly antiferromagnetic Fermi liquid (NAFL)³⁰ form, and the same parameters also arise in a renormalization group calculation of QCP's^{33,34}. Thus, evaluation of the parameters A , B , and C would amount to a *microscopic derivation of NAFL theory*. The present work evaluates these parameters in terms of two interaction parameters, the Hubbard U and a mode coupling parameter u . It is found that U has an important doping dependence, estimated in Appendix B, which is consistent with experiment. However, an attempt to directly calculate the mode coupling parameter u fails, giving anomalously small values – this problem has been noted previously, although there is debate about whether u diverges³¹ or vanishes^{33,34}. Here, the $t - J$ model is used to fix the value of u . Finally, it must be noted that the SCR theory is a model of weak ferro- or antiferromagnetism²⁵, and is here found to underestimate the Mott gap splitting near half filling. This most likely is due to imperfect self-consistency: the parameters are estimated from the bare susceptibility χ_0 , while the opening of the pseudogap leads to significant modifications of χ .

Despite these limitations, the resulting model is well behaved, and in good qualitative agreement with experiment, suggesting that a full derivation can ultimately be carried out along these lines. There are a number of *deviations* from the simplest NAFL theory. In Section III, it will be shown that the theory contains two additional *cutoff* parameters, q_c and ω_c^- , which cannot be neglected (or sent to infinity). One consequence of this is that the A parameter develops a significant temperature dependence, particularly in the electron-doping regime.

Equation 3, with $\text{Im}\chi \sim \omega$, only holds in the presence of hot spots³⁴. Hot spots complicate the evaluation of the A , B , and C parameters, since the expressions contain integrals which are formally divergent near the hot spots. For the present band structure, hot spots exist only when the chemical potential μ is in the range $4t' \leq \mu \leq 0$, or for doping $0.25 > x > -0.19$ (electron dopings are considered as negative).

The following section demonstrates how hot spots control the properties of the magnetic susceptibility (plateau formation), and summarizes the evaluation of the SCR parameters. The integrals are more singular at the end points of the hot spot range – the H and C points.

III. HOT SPOT PLATEAUS AND GENERIC QCPs

A. Plateaus in Doping Dependence

1. The Pseudo-VHS

The present analysis is based on a self-consistent renormalization scheme: in two dimensions, fluctuations prevent the establishment of long range AFM order. Hence, the relevant quantity on which the study is based is the bare magnetic susceptibility,

$$\chi_0(\vec{q}, \omega) = - \sum_{\vec{k}} \frac{f(\epsilon_{\vec{k}}) - f(\epsilon_{\vec{k}+\vec{q}})}{\epsilon_{\vec{k}} - \epsilon_{\vec{k}+\vec{q}} + \omega + i\delta}, \quad (4)$$

where δ is a positive infinitesimal. This susceptibility has been analyzed in a number of papers, but generally only $Im(\chi)$ is explored in detail (e.g., Refs. 47–49), whereas the Stoner criterion involves $Re(\chi)$, which was studied in Ref. 50. The extended discussion which follows is intended to bring out salient features for the computation of the NAFL parameters. The doping dependence of $\chi_0(\vec{Q}, \omega)$ is illustrated in Fig. 1a, where $\vec{Q} = (\pi, \pi)$. The susceptibility has a remarkable doping dependence, with the large peak at the Van Hove singularity (VHS) shifting⁵⁰ to half filling with increasing temperature T . The peak position of this ‘pseudo-VHS’ defines a temperature $T_V(x)$, Fig. 1d (circles). This behavior can readily be understood from the form of $\chi_0(\vec{Q}, 0)$, Eq. 4. The denominator $\epsilon_{\vec{k}} - \epsilon_{\vec{k}+\vec{Q}} = -4t(c_x + c_y)$, is *independent of t'* , and hence has a stronger divergence than the density of states (dos). Indeed, this divergence matches the strong VHS found for $t' = 0$ (perfect nesting), and like that VHS falls *at half filling*, $x = 0$. There is one crucial difference – at low temperatures, this divergence is *cut off* by the Fermi functions, which leave the integrand non zero in a wedge which intercepts the zone diagonal (where the denominator vanishes) only at isolated points: the hot spots. Hence, the residual divergence at low T is still dominated by the conventional VHS. However, *at finite T* , excitations along the zone diagonal become allowed, leading to a stronger divergence of $\chi_0(\vec{Q}, 0)$ near $x = 0$.

The strong temperature dependence of the pseudo-VHS is in strong contrast to the density of states, N_F , Fig. 1b, and also with the pairing correlations⁵⁰. The denominator of the pairing susceptibility involves the *sum* of the energies, $\epsilon_{\vec{k}} + \epsilon_{\vec{k}+\vec{Q}} = -8t'c_xc_y$, rather than their difference (as in Eq. 4), and hence always peaks at the ordinary VHS.

The difference between nesting and pairing susceptibilities has a fundamental significance. By mixing electron and hole-like excitations, the superconducting gap is always pinned to the Fermi level, and can open up a full gap at any doping. On the other hand, a nesting gap need not be centered on the Fermi surface, and is constrained to obey Luttinger’s theorem, conserving the net

number of carriers in the resultant Fermi surface. Hence, the only way a nesting instability (such as antiferromagnetism) can open a full gap at the Fermi level is for the instability to migrate with increased coupling strength to integer filling of a superlattice zone (e.g., half filling of the normal state).

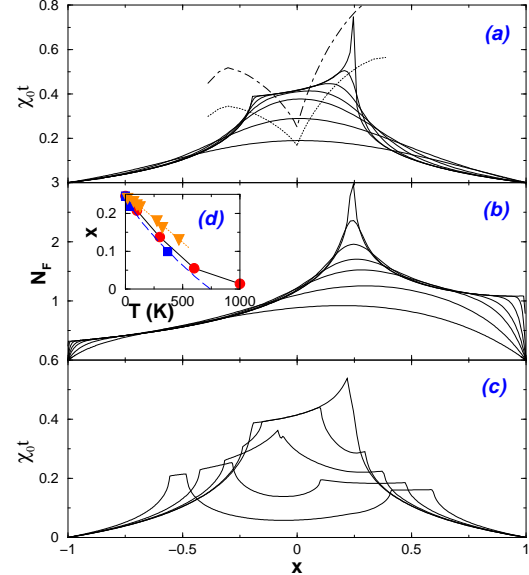


FIG. 1. (a) Susceptibility χ_0 at \vec{Q} as a function of doping for several temperatures. From highest to lowest curves near $x = 0.1$, the temperatures are $T = 1, 100, 300, 600, 1000, 2000$, and 4000 K. Dotted line = $1/U_{eff}$, dot-dashed line = $1.5/U_{eff}$. (b) Density of states N_F for the same temperatures. (c) Susceptibility χ_0 at \vec{Q} as a function of doping for several frequencies at $T = 1$ K: $\omega = 0.01, 0.1, 0.3, 0.6, 1.0$ eV. (d) Pseudo-VHS (peak of χ_0) as a function of temperature T_V (circles) or scaled frequency $T_c^- = \omega_c^-/\pi$ (squares); triangles = T_{incomm} .

Since the susceptibility has such a distinct *temperature* dependence from the density of states, one might ask how the *frequency* dependence compares. This is illustrated in Fig. 1c at low temperature (1K). While the frequency introduces additional sharp features and has an overall very distinct appearance from the T-dependence, nevertheless the main peak also shifts from the VHS toward lower doping with increasing ω – in fact, the shift is almost the same when comparing $\hbar\omega$ and $\pi k_B T$, Fig. 1d. The dashed line in Fig. 1d is $T_c^- = \hbar\omega_c^-/\pi k_B$, with⁴⁷

$$\omega_c^- = \frac{4t(\hat{\mu} - \tau)}{1 - \tau}, \quad (5)$$

with $\tau = 2t'/t$ and $\hat{\mu} = \mu/2t$. The proportionality of frequency and temperature dependences holds only in the hole doped regime: temperature shifts the susceptibility peak only to half filling, $x = 0$, while frequency will shift the peak beyond half filling ($x < 0$).

Also in contrast to N_F , the susceptibility has (at low T) a plateau shape, with sharp falloff in intensity beyond

the plateau edges on both electron and hole doping sides of half filling. This shape is characteristic of hot spot physics. Hot spots are those points where the Fermi surface (FS) intersects the replica FS shifted by \vec{Q} . They are located at $c_x = -c_y = c_{x0}$, with

$$c_{x0} = \cos ak_{x0} = \sqrt{\frac{\mu}{4t'}}, \quad (6)$$

and equivalent points. The edges of the plateau are those points at which the overlap terminates (hot spots cease to exist). For the band structure of Eq. 1 these points occur at chemical potential $\mu = 4t' \equiv \mu_v$ (the VHS) and 0, or at dopings $x = 0.25, -0.19$ (taking electron dopings as negative). Since these two end points play an important role, it is convenient to label them, and they are here called ‘hot’ hot spot and ‘cold’ hot spot (or H-point and C-point) for the hole and electron-doped termination points, respectively. It will be demonstrated below that at each doping, the hot spots also lead to a susceptibility plateau in momentum space, around \vec{Q} , collapsing to a logarithmic (square root) divergence at the H- (C)-point. The H-point is the VHS, and hence also involves a conventional ETT. The physics is simpler near the C-point, where the topology hardly changes but the FS and \vec{Q} -FS become decoupled (it is therefore a form of Kohn anomaly⁵⁰).

2. Mean Field Mott Transition

For the parameter values expected in the cuprates, these susceptibility plateaus control the physics of the Mott gap collapse²⁰. As a function of doping, the mean field Mott gap is found to close at a doping just beyond the edge of the plateau, *for both electron and hole doping*, Fig. 2. The solid and long dashed lines are the commensurate and incommensurate mean field Mott transition temperatures $T^*(x)$ calculated using the estimated $U_{eff}(x)$, dotted line in Fig. 1. For electron doping, there is a double transition, first from commensurate to incommensurate antiferromagnetic order at the plateau edge, then to the loss of any magnetic order at a slightly higher doping (inset a). For hole doping, the dominant antiferromagnetic order is incommensurate for all dopings, but the difference in T_N becomes significant only near the H-point (inset b). When fluctuations are included (below), it is found that the Néel transition is shifted to zero temperature, while a pseudogap first appears near the mean field T_N . Interlayer coupling can then restore a finite T_N , Section V. For the real cuprates, the terminations of the Mott gaps are preempted by superconducting transitions, close to the critical regime.

While the present local calculation (minimizing the free energy at a fixed doping) finds incommensurate magnetic order for hole doping, some global calculations (comparing free energies over a wider doping range) find that this is precluded by a phase separation instability.

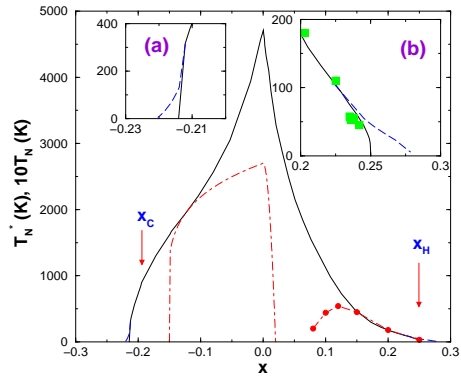


FIG. 2. Mean field magnetic transition temperatures determined from Stoner criterion using U_{eff} of Fig. 1. Solid line: commensurate (at \vec{Q}); long dashed line: incommensurate. Dot-dashed line = $10T_N$, where T_N is the onset of long range AFM order, from [51] and [52] (with filled circles). Insets = blowups near C- and H-points. Squares in inset b = pseudogap data of [53].

The structure in the low temperature susceptibility, Fig. 1, with its largest peak at the H-point on the hole doped side, is in striking contrast to the calculated doping dependence of the Néel transition, Fig. 2, which has a broad plateau on the electron-doped side, but falls off more quickly with hole doping, showing no sign of a peak near the VHS. This contrast can be accounted for by two effects. First, the shift of spectral weight with temperature of the pseudo-VHS, noted in Fig. 1, would tend to produce a symmetric falloff of T_N with either electron or hole doping. But the dos peak at the VHS leads to better screening of U_{eff} for hole doping, thereby further depressing T_N . The experimentally observed⁵¹ T_N (dot-dashed line) shows an even stronger falloff with hole doping, perhaps due to phase separation. Since stripes can frustrate magnetic order, the figure also includes the magnetic ordering temperature of quasi-static stripe arrays, from Nd-substituted LSCO⁵², which is taken as a lower bound for the Néel ordering transition in the absence of stripes. The mean field calculation provides an approximate envelope of the resulting data, but overestimates the transition temperatures by a factor of 10. Note that in the hole doped regime, there is good agreement between the mean field transition and the pseudogap²⁰ (squares in Fig. 1b = data of Krasnov⁵³, assuming $2\Delta = 4.6T^*$). Calculation of the Néel transition beyond the mean field level will be discussed in Section V.

B. Plateaus in Momentum Space

1. Plateaus

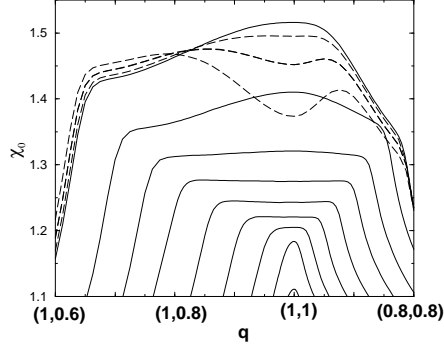


FIG. 3. Susceptibility χ_0 near \vec{Q} for a variety of dopings at $T = 100K$. From highest to lowest solid curves near $S \equiv \vec{Q}$, the chemical potentials are $\mu = -0.35, -0.30, -0.25, -0.20, -0.15, -0.10, -0.055, -0.02$, and 0 eV. For the dashed curves (top to bottom), $\mu = -0.352, -0.355$, and -0.359 eV.

In analyzing either thermal fluctuations or the quantum fluctuations associated with QCPs, it is necessary to understand the susceptibility near the AFM vector \vec{Q} . At each doping, hot spot physics leads to a plateau in momentum space, centered on \vec{Q} . Figure 3 shows how χ_0 varies near \vec{Q} at a low temperature (100K) for a series of different dopings. Results near $T = 0$ are presented in Ref. 35. For all dopings there is a plateau in q . The width of the plateau at $T = 0$ can be readily determined²⁰: in any direction, it is the minimum q needed to shift the replica FS so that the hot spots are eliminated. This can be found from the dispersion, Eq. 1, by substituting $\vec{k} \rightarrow (\vec{Q} + \vec{q})/2$, or

$$-2t(\hat{s}_x + \hat{s}_y) - 4t'\hat{s}_x\hat{s}_y = \mu, \quad (7)$$

with $\hat{s}_i = \sin(q_i a/2)$. As shown in Fig. 4, this formula agrees with the (anisotropic) plateau width measured from Fig. 3 (circles). The inset shows the shape of the plateau as a function of doping. The diamond shape of the plateau, Eq. 7, is related to the profile of the hole pockets formed by the overlap of the shifted and unshifted FSs. Specifically, the plateau is the region of overlap of the two hole pockets, shifted to have a common center, as illustrated in Fig. 5. The remaining parts of the pockets also show up, as ridges⁵⁴ in the susceptibility, radiating from the corners of the diamond (similar to the peaks in the $\mu = 0.05$ eV data in Fig. 6, below). As noted by Bénard, et al.⁴⁷, the susceptibility in two-dimensions acts as a FS caliper. The plateau width leads to a natural limit on the magnetic correlation length, $\xi_c \sim 1/q_c$, in agreement with experimental data⁵⁵ (squares in Fig. 4), as noted previously^{49,50}.

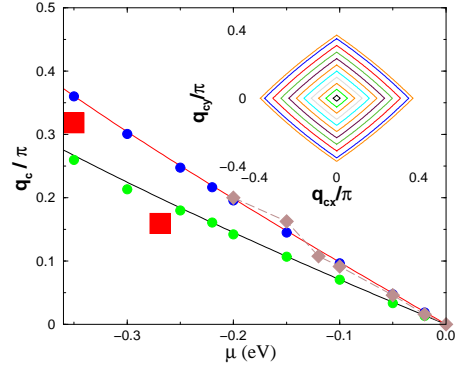


FIG. 4. Plateau width q_c , comparing Eq. 7 (solid lines) and the measured widths (circles) from Fig. 3. Upper curve along $[q_c, 0]$ direction, lower along $[q_c, q_c]/\sqrt{2}$ direction. Squares = experimental inverse correlation lengths ξ^{-1} from Ref. 55; diamonds = $T_A^*/5000K$. Inset = plateau boundary for a series of chemical potentials μ from 0 (smallest) to -0.359 eV (largest).

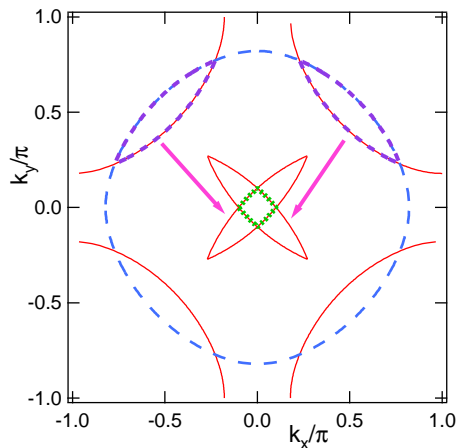


FIG. 5. Illustrating origin of plateaus (dotted line) from crossed hole pockets (short dashed lines).

The plateaus in q help in understanding the doping dependence of the susceptibility near \vec{Q} , Fig. 1a. At each doping on the plateau (in x) there is a plateau in q centered at \vec{Q} , with the width of the plateau decreasing to zero as $x \rightarrow x_C$, Fig. 6. The critical points $q = q_c$ are precisely those points at which the $\vec{Q} + \vec{q}$ -shifted-FS no longer overlaps the original FS.

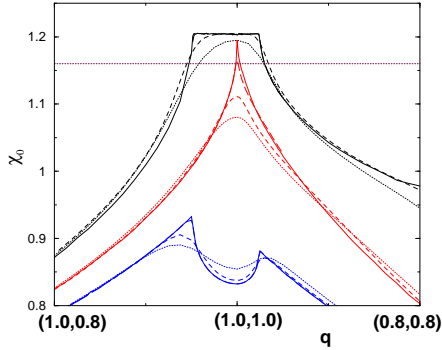


FIG. 6. Susceptibility χ_0 near \vec{Q} for several dopings near the C-point. Upper group at $\mu = -0.05\text{eV}$, middle at $\mu = 0$ (C-point), and bottom at $\mu = +0.05\text{eV}$. Temperatures are $T = 200\text{K}$ (dotted lines), 100K (short dashed lines), 10K (long dashed lines), 1K (solid lines). Horizontal line = $U_{\text{eff}}(\mu = 0)$.

2. Cusps

For electron-doping beyond the C-point ($\mu > 0$), the plateau ends and the susceptibility displays split peaks away from \vec{Q} , Fig. 6, with a dip in between. The change in character of χ_0 means that $\mu = 0$ is a QCP. (The corresponding QCP at the H-point was analyzed in Ref. 50.) However, the *magnitude* of χ_0 also changes rapidly near $\mu = 0$, so there should be a transition to a non-magnetic phase near the same doping²⁰, as discussed in the previous subsection (note the line depicting $U(\mu = 0)$ in Fig. 6).

The origin of these $\mu > 0$ *cusps* can be readily understood from Fig. 7. Here, the contributions of individual quadrants to the χ integral are plotted separately, with each quadrant containing two hot spots. It can be seen (Appendix D) that the dispersion at *each* hot spot contains a cusp, near which the dispersion is linear in $|q|$. However, when adding the contributions of the 8 hot spots, the linear terms cancel, leaving a quadratic dispersion. For $\mu > 0$ and $q = 0$ there are no hot spots – the Fermi surfaces in \vec{k} and $\vec{k} + \vec{Q}$ do not intersect. However, translating one Fermi surface by \vec{q} will lead to an intersection, with corresponding hot spot, beyond some threshold \vec{q}_c . Since only one or two hot spots are restored for a given direction of \vec{q}_c , the linear terms do not cancel, leading to a linear in q dispersion for $q > q_c$. Exactly at $\mu = 0$, χ_0 has a \sqrt{q} cutoff as $q \rightarrow Q$ (Appendix D3).

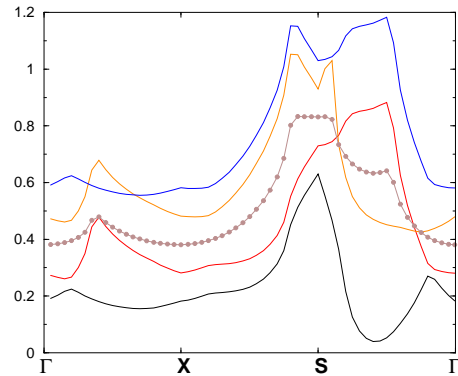


FIG. 7. Bare susceptibility χ_0 , for $x = 0$, (beaded line); various solid lines show contributions of individual quadrants, shifted vertically by 0.1 for clarity. The special points in the Brillouin zone are $\Gamma = (0,0)$, $X = (\pi,0)$, and $S = \vec{Q}$. ($T = 100\text{K}$.)

Technically, similar cusps also arise at the plateau edges²⁰ for electron doping, $0 > \mu > -0.22\text{eV}$. The tops of the plateaus are not completely flat, Fig. 8a: the highest susceptibility is shifted away from \vec{Q} , and the sharp steps near \vec{Q} are again hot spot effects, this time associated with the loss of hot spots at large values of $\vec{q} - \vec{Q}$. However, these effects are much weaker than those associated with $\mu > 0$ ($\Delta\chi/\chi \leq 0.5\%$ – compare the vertical scales of Figs. 6, 8). Thus near the mean-field transition any structure on the plateaus is smeared out by thermal broadening. Even at $T = 0$, these features are likely to be negligible compared to dispersion in U which arises from renormalization effects⁵⁶.

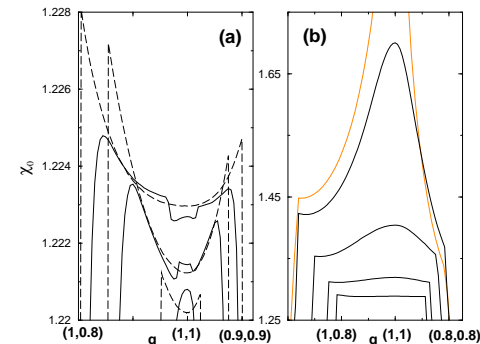


FIG. 8. (a): Expanded view of susceptibility χ_0 on the plateaus near \vec{Q} for a variety of dopings at $T = 100\text{K}$ (solid curves) or 1K (dashed curves). From highest to lowest curves near \vec{Q} , the chemical potentials are $\mu = -0.20, -0.15$, and -0.05 eV (for both solid and dashed curves). All curves except $\mu = -0.20\text{eV}$ have been shifted vertically to fit within the expanded frame. (b): Similar plateaus for the hole doped materials ($T = 1\text{K}$), with (from highest to lowest) $\mu = -0.359, -0.35, -0.3, -0.25$, and -0.22 eV .

3. Curvature (A)

The plateau is a region of anomalously small local curvature $\hat{A} = A/U$ (Eq. 2) of the susceptibility, $\chi_0(\vec{Q} + \vec{q}) = \chi_Q - \hat{A}q^2$, where A is an important NAFL parameter. Clearly, at $T = 100K$ the curvature A has gone negative near the H -point, Fig. 3. At even lower temperatures, it reverts to positive values, Fig. 8b. The temperature dependence of the normalized parameter $A' = (\pi/a)^2(U/t)A$ is illustrated in Fig. 9 at several dopings. The temperature dependence is dominated by divergences at both H - and C -points. The divergence at the H -point Fig. 9a is the well-known logarithmic VHS. However, at finite temperatures spectral weight is shifted away from the VHS and A turns negative, only recovering a positive sign above $T \simeq 2000K$. The temperature at which A turns negative can be defined as T_{incomm} : $A < 0$ for $T > T_{incomm}$. From Fig. 1d, T_{incomm} is comparable to but larger than T_V (for $x \leq 0.06$ A remains positive). This in fact explains the origin of T_{incomm} . Figure 9a demonstrates that A is negative at $T \rightarrow 0$ beyond the H -point ($\mu = -0.4eV$). Thus, increasing T above T_V produces the same susceptibility crossover. A similar crossover was discussed by Sachdev, et al.⁵⁷, except that they assumed that in the high temperature phase the AFM fluctuations remained centered on the commensurate \vec{Q} , whereas here A is negative. At sufficiently high temperatures A again becomes positive for all dopings – i.e., the leading singularity of χ_0 is always at \vec{Q} .

At the C -point, the collapse of the plateau width translates into a divergence of the curvature at \vec{Q} ($\hat{A} \rightarrow \infty$). This divergence of the high-temperature susceptibility is cut off at low T , Fig. 9d, when the thermal smearing becomes smaller than the plateau width. For smaller T , A is controlled by the curvature on the plateau. The temperature at which A has a peak, defined as T_A^* , is plotted as diamonds in Fig. 4 (the peak is only found for $x \leq 0$). Rather surprisingly, T_A^* scales with the plateau width q_c , even though the dynamic exponent is $z = 2$. Further, the maximum slope scales approximately as $A_{max} \sim T_A^{*-1.5}$, which follows from the fact that $A \sim T^{-1.5}$ at the C -point.

At intermediate doping, Fig. 9b,c, A is generally a scaled-down version of the behavior near the two end points, with a crossover near $\mu = -0.25eV$, where the T -dependence is weak. Also for intermediate temperatures, there can be fine structure on the plateau (e.g., solid lines in Fig. 8a) which can lead to wild swings in $A(T)$. However, at these dopings they are not relevant, since the susceptibility peaks are away from \vec{Q} , and this fine structure is not generally reported in Fig. 9.

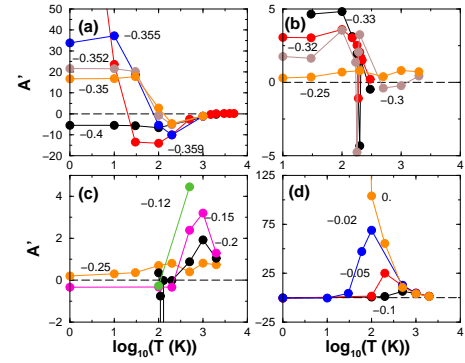


FIG. 9. Temperature dependence of A' for several dopings.

C. Plateaus in Frequency

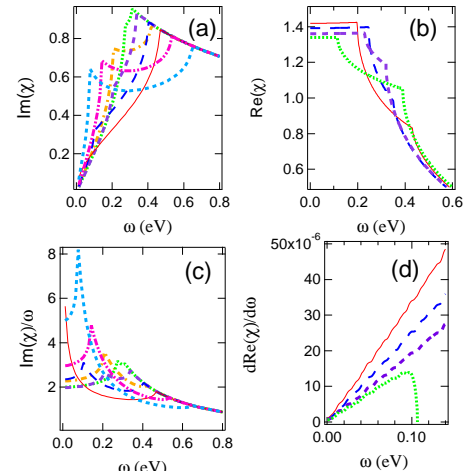


FIG. 10. (a) $Im\chi(\vec{Q}, \omega)$, (b) $Re\chi(\vec{Q}, \omega)$, (c) $Im\chi/\omega \equiv \hat{C}$, and (d) $dRe\chi(\vec{Q}, \omega)/d\omega$, for (a,c): $\mu = 0$ (solid line), -0.05 (long dashed line), -0.10 (dashed line), -0.15 (dotted line), -0.20 (dot-dashed line), -0.25 (dot-dot-dashed line), and -0.30eV (short dashed line); (b,d): $x = 0$ (solid line), 0.04 (long dashed line), 0.10 (dashed line), and 0.15 (dotted line).

Figure 10 illustrates $Im\chi(\vec{Q}, \omega)$, $Re\chi(\vec{Q}, \omega)$, and $Im\chi/\omega \equiv \hat{C}$. At $T = 0$, the imaginary part of the susceptibility $\chi(\vec{Q}, \omega)$ can be calculated analytically⁴⁷:

$$Im(\chi(\vec{Q}, \omega)) = \sum_{\vec{k}} (f(\epsilon_{\vec{k}}) - f(\epsilon_{\vec{k}+\vec{Q}})) \delta(\epsilon_{\vec{k}+\vec{Q}} - \epsilon_{\vec{k}} - \omega) = \frac{F(\theta_1, \tilde{k}) - F(\theta_2, \tilde{k})}{4t}, \quad (8)$$

where $F(\theta, x)$ is an elliptic integral, $\tilde{k} = \sqrt{1 - (\omega/8t)^2}$, and $\sin(\theta_i) = \sin(\phi_i)/\tilde{k}$, with

$$\cos^2(\phi_1) = \begin{cases} c_-^2 & \text{if } \omega \leq \omega_c^- \\ \hat{\omega}/2 & \text{if } \omega > \omega_c^- \end{cases}, \quad (9)$$

$$\cos^2(\phi_2) = \begin{cases} c_+^2 & \text{if } \omega \leq \omega_0, \\ 1 & \text{if } \omega > \omega_0 \end{cases}, \quad (10)$$

with $\hat{\mu} = \mu/2t$, $\hat{\omega} = \omega/4t$, $c_\pm^2 = a_\pm + \sqrt{a_\pm^2 - \hat{\omega}^2}$, and $a_\pm = 1 - (\hat{\mu} \pm \hat{\omega})/\tau$. The real part $Re\chi$ can be found from the Kramers-Kronig result,

$$Re\chi(\vec{Q}, \omega) = \frac{1}{\pi} \int_0^\infty \frac{Im\chi(\vec{Q}, \omega') \omega' d\omega'}{\omega'^2 - \omega^2}. \quad (11)$$

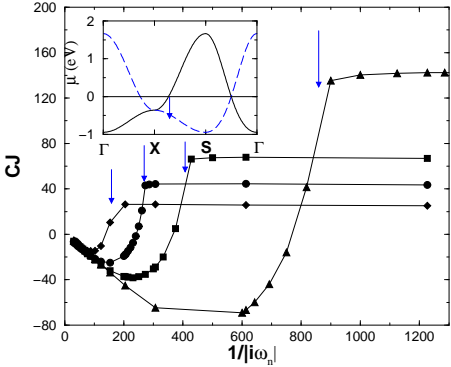


FIG. 11. \hat{C} calculated for several values of μ : $\mu = -0.355$ (diamonds), -0.357 (circles), -0.358 (squares), -0.359 eV (triangles) [$\mu_v = -0.359$ eV]. Inset: Band dispersion $\epsilon_{\vec{k}}$ (solid line) $\epsilon_{\vec{k}+\vec{Q}}$ (dashed line), for $\mu = 0$. Arrow = ω_c^- .

Thus, there are also plateaus in the frequency dependence of $Re\chi$. Furthermore, hot spots generate an imaginary part of the susceptibility linear in frequency, which also approximates a plateau, particularly near the H-point, Fig. 11. The origin of this plateau and of the critical frequencies ω_c^- , Eq. 5, and

$$\omega_0 = \frac{8t}{\tau} [\sqrt{1 - \hat{\mu}\tau} - 1] \quad (12)$$

can be understood from Fig. 12. The thick (thin) solid lines represent the original (Q-shifted) Fermi surfaces, while the dashed lines represent

$$\omega = \epsilon_{\vec{k}+\vec{Q}} - \epsilon_{\vec{k}}, \quad (13)$$

for various values of ω . Equation 13 gives the points at which the denominator of $\chi_0(\vec{Q}, \omega)$, Eq. 4, vanishes. Thus at $T = 0$, $Im(\chi_0(\vec{Q}, \omega))$ is proportional to the length of the dashed line lying between the original and Q-shifted FSs (i.e., where $f(\epsilon_{\vec{k}}) - f(\epsilon_{\vec{k}+\vec{Q}}) = \pm 1$). Since the two FSs meet at an angle, forming a wedge, $Im(\chi_0(\vec{Q}, \omega)) \sim \omega$.

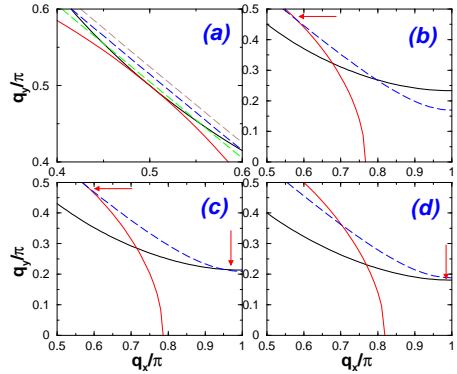


FIG. 12. Origins of critical cutoffs. Thick solid line = FS; thin solid line = Q-shifted FS; dashed lines = Eq. 13, for several values of ω . Chemical potential μ = (a) 0, (b) -0.1 , (c) -0.14 , (d) -0.2 eV. horizontal arrows indicate ω_0 , vertical arrows ω_c^- .

From Fig. 12, the critical frequencies (denoted by arrows) are points where the ω dependence of this length changes abruptly, leading to a sharp change in $Im\chi$. Thus, near the H-point, the plateau width is ω_c^- (inset, Fig. 11), while near the C-point it is ω_0 . The vertical arrows in Fig. 12 indicate ω_c^- , where the dashed line (Eq. 13) intersects the FS at the zone boundary, while the horizontal arrows are⁴⁷ ω_0 , where the dashed line ceases to intersect the Q-shifted FS. There is a crossover at $\mu_c \simeq -0.14$ eV: for $\mu > \mu_c$, $\omega_0 < \omega_c^-$ while for $\mu < \mu_c$, $\omega_0 > \omega_c^-$. Combining Eqs. 5, 12, $\omega_0 = \omega_c^-$ at $\mu_c = [1 - z(2 - \sqrt{z})^2]2t/\tau = -0.1384$ eV, with $z = 1 - \tau$. For $\omega > \min\{\omega_0, \omega_c^-\}$, $Im(\chi_0(\vec{Q}, \omega)) \sim \omega^{1/2}$, so $C \sim 1/\omega^{1/2}$ – i.e., the susceptibility is no longer on the plateau.

The height of the plateau C is an important parameter of the SCR model. It can be represented as another frequency $\omega_1 = 1/C$, with $C = U\hat{C}(\omega = 0)$. From Eq. C22 of Appendix C2, C can be found explicitly

$$C = \frac{1}{2\pi J s_{x0}^2 (1 + \tau c_{x0})} = \frac{1}{\omega_1} \quad (14)$$

(with $J = 4t^2/U$, $s_{x0}^2 = 1 - c_{x0}^2$). Defining a width parameter $\alpha_\omega = \min\{\omega_c^-, \omega_c^0\}$, with $\omega_c^0 = \omega_0/\omega_1$, then

$$\omega_1/\omega_c^- = \frac{2\pi t(1 - \tau)}{U} \frac{1 + \tau c_{x0}}{-\tau} \equiv \frac{1}{\alpha_\omega^-}. \quad (15)$$

This latter is in good agreement with the numerical results (arrows in Fig. 12) and is similar to the result found by Onufrieva and Pfeuty⁵⁰, using a hyperbolic band approximation valid near a VHS, $\omega_1/\omega_c^- = 2\pi t(1 - \tau)/U$.

Because of the dynamic scaling $\omega \sim q^z$, this crossover is also reflected in the behavior on the plateau in \vec{q} , Fig. 8: for $\mu > -0.14$ eV, the plateau has a negative curvature, which can almost be scaled between different dopings, while for $\mu < -0.14$ eV, the plateau starts to fill in, ultimately developing a peak at \vec{Q} . (See also Fig. 3a in

Ref. 35.) Note that the plateau width collapses in frequency at both the H - and C -points, while the collapse in wave number ($q_c \rightarrow 0$) is only present near the C -point.

D. Parameter Evaluation for Mode Coupling Theory

The evaluation of the SCR parameters A and C was discussed above. The collapse of the \vec{q} and/or ω plateau widths near the H - and C -points leads to the introduction of additional parameters q_c and α_ω . The narrow width of the \vec{q} -plateau, particularly for electron doping, leads to an additional complication not included in the conventional SCR analysis: the curvature of the bare susceptibility near $\vec{Q} = (\pi, \pi)$ (the S -point of the BZ) is strongly temperature dependent, and for some dopings may even change sign. In principle, it is not difficult to incorporate an $A(T)$ into the analysis near the mean-field Néel temperature T_N^* (pseudogap onset). But for the present 2D system, long range Néel order only sets in at $T_N = 0$, and for $T \ll T_N^*$, a self consistent value of A should be found, by taking into account the effect of the pseudogap in modifying the electronic dispersion and hence χ . For the present, this complication is ignored, and in the following section A is taken as $A = A(T_N^*)$, where T_N^* is the magnetic pseudogap onset, the temperature where $\chi_0(\vec{Q})U_{eff} = 1$, using the effective U_{eff} found earlier¹¹ (Appendix B). This should be the most important A for controlling the pseudogap, and moreover at lower temperatures the band renormalization should strongly modify $A(T)$. With this choice, the resulting $A(\mu)$ is plotted in Fig. 13, along with the C parameter, evaluated at $T = 0$. Note that for electron doping, this choice of A is always positive and varies smoothly with doping, diverging at the C -point. By contrast, for hole doping A is often negative, again illustrating the instability of the uniform AFM phase. [In principle, a positive A can be found by taking an incommensurate nesting vector; for this paper, only commensurate nesting is considered; the negative A will suggest when electronic inhomogeneity may be important.] Given A and C , Fig. 14 shows the calculated values of $\chi_{\vec{Q}}$ and ω_{sf} , normalized to ξ^2 .

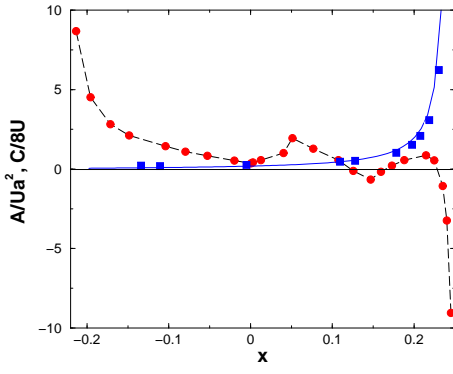


FIG. 13. Calculated values of A (circles) and C (squares), for $U = 6t$. Solid line = Eq. 14

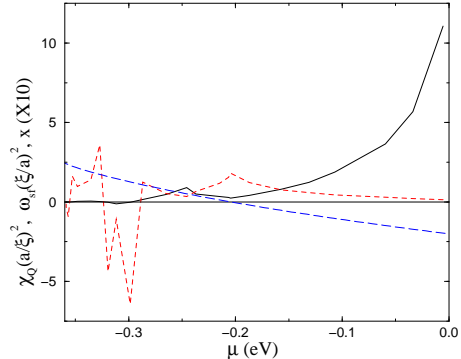


FIG. 14. Calculated values of $\chi_{\vec{Q}}/\xi^2$ (solid line) and ω_{sf}/ξ^2 (short dashed line), assuming $U = 6t$. Long dashed line = doping $x(\mu)$ ($\times 10$).

In the following, the present results are applied to understanding the ARPES spectra of electron doped cuprates, concentrating on the four dopings analyzed by Armitage, et al.¹⁰. For convenience, Table I summarizes the parameters for these dopings. From the mean-field analyses¹¹, the effective Hubbard parameters were found to be $U_{eff}/t = 6$ ($x = 0$), 5 ($x = -0.04$), 3 ($x = -0.10$), and 2.5 ($x = -0.15$). [These numbers differ somewhat from those of Ref. 11, since a second neighbor hopping, t'' , was included in the latter analysis, to give the best fit of the Fermi surfaces.] The Stoner factor has a quantum correction, η , Eq. C34, which tends to suppress the AFM transition; hence a smaller renormalization of U is required. This is reflected in Table 1: for $x = -0.1, -0.15$, there are two rows, the upper row using the mean-field U parameters, the lower with the quantum correction. Note that the U 's are enhanced by essentially the quantum correction factor. These values will be used in the subsequent analysis.

The SCR analysis also involves a mode coupling parameter u , evaluated in Appendix D6. As found previously, direct evaluation of this parameter is unsatisfactory – the results of Table 1 being anomalously small due to the flatness of the susceptibility plateau ($\partial\chi/\partial\omega \sim 0$), Fig. 10d. Below, an empirical way to estimate u is suggested.

Table I: Electron Doped Cuprates

x	U/t	A/a^2	ω_1 (eV)	α_ω	$q_c a$	η	$T_A^*(K)$	u^{-1} (eV)
0	6	0.696	0.345	0.583	0.635	1.29	1020	760
-0.04	5	1.16	0.540	0.455	0.518	1.25	850	3200
-0.10	3	1.34	1.32	0.176	0.342	1.19	500	2700
"	3.5	1.56	1.13	0.206	"	1.24	"	2300
-0.15	2.5	1.75	2.16	0.054	0.172	1.08	56	4000
"	2.9	2.03	1.86	0.062	"	1.15	"	3500

It is convenient to compare the present results with

parameters estimated for the SCR model²⁹ from experimental data for (optimally) hole-doped cuprates. The parameters are defined as $T_0 = Aq_B^2/2\pi C$, $T_A = Aq_B^2/2\chi_0$, $y_0 = \delta_0(T=0)/Aq_B^2$, and $y_1 \simeq 12a^2u/\pi^3 AC$. The results are listed in Table II, where the first line gives the hole-doped results estimated in Ref. 29. Moriya, et al.²⁹ took $q_B^2 = 1/4\pi a^2$ ($q_B a = 0.282$), while for Table II it is assumed that $q_B = q_c$. A key difference is that Moriya, et al.²⁹ assume the system is in the paramagnetic phase ($y_0 > 0$) at and above optimal (hole) doping, while in the present work $y_0 < 0$, and the system is paramagnetic due to the Mermin-Wagner theorem, with the Mott gap appearing as a pseudogap. The small magnitude of y_0 is suggestive of a system pinned close to a QCP. Finally, the parameter y_1 is estimated using the value $u^{-1} = 0.256\text{eV}$ (below), and not the anomalous values of Table 1.

Table II: SCR Parameters

x	T_0 (K)	T_A (K)	y_0	y_1
~0.2	1600-4000	3000-10000	0.01-0.02	3
0.0	180	1150	-5.27	0.75
-0.04	310	1300	-3.31	0.7
-0.10	380	670	-1.23	1.5
-0.15	200	220	-0.31	1.85

IV. ARPES SPECTRA

A. SCR Transition and Correlation Length

Given the above parameters, the doping dependence of the MF and SCR transitions is compared in Fig. 15 for the four electron dopings studied in Refs. 10, 11. The MF transition occurs when the bare Stoner factor $\delta_0 = 1 - \chi_{\vec{Q}0}U$ becomes negative, Fig. 15a. However, in SCR the renormalized Stoner factor δ stays positive, so there is no $T > 0$ phase transition (Mermin-Wagner theorem), although $\delta - \delta_0$ has a strong increase near the temperature where δ_0 changes sign. There is still a zero-T Néel transition, controlled by the quantum corrected Stoner factor, $\bar{\delta}_0 = \eta - \chi_{\vec{Q}0}U$. From Fig. 15c, it can be seen that at $x = -0.15$, the system is close to a QCP, $\bar{\delta}_0(T=0) \rightarrow 0$. This QCP is controlled by the Stoner criterion of the zero-T antiferromagnet. While there is no long range order, there is still a Mott (pseudo)gap, controlled by *short-range* order, Fig. 15d. This will be discussed further below.

In the renormalized classical regime, the vanishing of δ as $T \rightarrow 0$ is controlled by a correlation length, which can be written as⁵⁸

$$\xi = \xi_0 e^{2\pi\rho_s/k_B T} \quad (16)$$

with spin stiffness ρ_s given by Eq. C44. The prefactor ξ_0 is T -dependent, $\xi_0 = \sqrt{Ae/2CT}$. This T -dependence agrees with the *one-loop* σ -model results⁵⁹ rather than the more accurate two-loop results^{58,60}. This difference

is presumably a deficiency of the present model in not using fully self consistent parameters. Note that ρ_s is found to be nearly T -independent below the pseudogap onset. Equation 16 is used to fix the value of u . From Eq. C44, $\rho_s \propto u^{-1}$, while the σ -model calculations^{58,59} give $\rho_s = JS^2$. Equating these two expressions for $x = 0$, $T = 0$ gives $u^{-1} = 0.256\text{eV}$, which is assumed for all dopings. The calculated values of ρ_s are illustrated in Fig. 15c, based on Eqs. C45, C44.

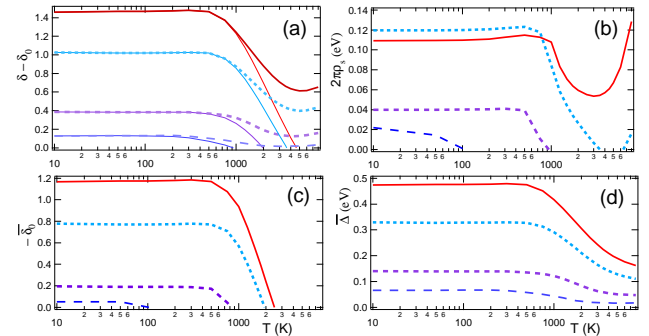


FIG. 15. (a) $\delta - \delta_0$ (thin solid lines = $-\delta_0$); (b) ρ_s calculated from Eqs. C44, C38; (c) $-\bar{\delta}_0$; (d) $\bar{\Delta}$, Eq. 22. In all the plots, the solid curves correspond to $x = 0.0$, dotted lines: $x = -0.04$, short dashed lines: $x = -0.10$, long dashed lines: $x = -0.15$.

B. General Results

Given the susceptibility, Eq. 3, the self energy can be calculated as

$$\begin{aligned} \Sigma(\vec{k}, i\omega_n) &= \frac{g^2\chi_0}{\beta V} \sum_{\vec{q}, i\omega_m} G_0(\vec{k} + \vec{q}, i\omega_n + i\omega_m) D_0(\vec{q}, i\omega_m) \\ &= \frac{g^2\chi_0}{V} \sum_{\vec{q}} \int_{-\alpha_\omega/C}^{\alpha_\omega/C} \frac{d\epsilon}{\pi} \frac{n(\epsilon) + f(\xi_{\vec{k}+\vec{q}})}{i\omega_n + \epsilon - \xi_{\vec{k}+\vec{q}}} \frac{C\epsilon}{(\delta + Aq'^2)^2 + (C\epsilon)^2}, \end{aligned} \quad (17)$$

with bare Green's function $G_0(\vec{k}, i\omega_n) = 1/(i\omega_n - \xi_{\vec{k}})$ and magnetic propagator D_0 , Eq. C26; for the form of the integral, see the discussion near Eq. C33. In addition, $\chi_0 = \chi_0(\vec{Q}, 0)$, $\vec{q} = \vec{Q} + \vec{q}'$, n is the Bose function, and

$$g^2\chi_0 = U^2\chi_0(U\chi_0(\vec{Q}, i\omega_n) + \frac{1}{1 + U\chi_0(\vec{Q}, i\omega_n)}) \simeq \frac{3U}{2} \quad (18)$$

(Ref. 61). The last form is an approximation based on the empirical substitution $\chi_0 \rightarrow \simeq 1/U$ in the pseudogap regime. After analytical continuation, the imaginary part of the retarded self energy is

$$\begin{aligned} Im\Sigma^R(\vec{k}, \omega) &= \frac{-g^2\chi_0}{V} \sum_{\vec{q}} \int_{-\alpha_\omega/C}^{\alpha_\omega/C} d\epsilon [n(\epsilon) + f(\xi_{\vec{k}+\vec{q}})] \times \\ &\times \delta(\omega + \epsilon - \xi_{\vec{k}+\vec{q}}) \frac{C\epsilon}{(\delta + Aq'^2)^2 + (C\epsilon)^2}. \end{aligned} \quad (19)$$

The resulting self energy is plotted in Fig. 16 for $T = 100K$. (The weak oscillations seen in some branches of Σ_I are an artifact due to an insufficient density of points in the numerical integration.) Note that $Im\Sigma$ has the form of a broadened δ -function peaked at $\omega = \xi_{\vec{k}+\vec{Q}}$. If it were a δ -function, $Im\Sigma = -\pi\bar{\Delta}^2\delta(\omega - \xi_{\vec{k}+\vec{Q}})$, then

$$Re\Sigma^R(\vec{k}, \omega) = \frac{1}{\pi} \int_{-\infty}^{\infty} d\epsilon \frac{Im\Sigma^R(\vec{k}, \epsilon)}{\epsilon - \omega} = \frac{\bar{\Delta}^2}{\omega - \xi_{\vec{k}+\vec{Q}}}, \quad (20)$$

so away from the δ -function

$$G(\vec{k}, \omega) = \frac{1}{\omega - \xi_{\vec{k}} - Re\Sigma^R(\vec{k}, \omega)} = \frac{\omega - \xi_{\vec{k}+\vec{Q}}}{(\omega - \xi_{\vec{k}})(\omega - \xi_{\vec{k}+\vec{Q}}) - \bar{\Delta}^2}. \quad (21)$$

This is exactly the Green's function of the mean field calculation^{1,13}, with the substitution $\Delta \rightarrow \bar{\Delta}$, where $\bar{\Delta}$ can be evaluated by integrating

$$\begin{aligned} \bar{\Delta}^2 &= -\frac{1}{\pi} \int_{-\infty}^{\infty} d\omega Im\Sigma^R(\vec{k}, \omega) \\ &= \frac{U}{8u}(\delta - \delta_0), \end{aligned} \quad (22)$$

Fig. 15d. This result is due to the Bose term $n(\epsilon)$ in the square bracket of Eq. 19, the Fermi function f making no contribution. This leads to $\bar{\Delta}$ being independent of \vec{k} .

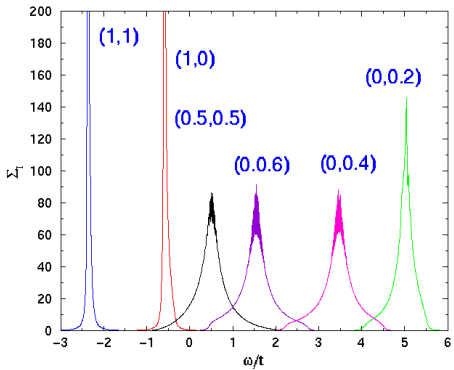


FIG. 16. Imaginary part of the self energy, Eq. 19, assuming $1/C = 0.05t$, $\delta = 0.002$, $\alpha_\omega = 1$, $T = 100K$. The branches are labelled (k_x, k_y) , in units of π .

Equations 21,22 constitute an important result: the connection between the Mott gap and short-range magnetic order. Recalling that $\Delta = U < M_i >$, or $\Delta^2 = U^2 < S_i >^2$, where $< M_i > = (-1)^i < S_i >$ is the staggered magnetization, then, in the spirit of an alloy analogy, a *short-range order parameter* can be defined as

$$\begin{aligned} \bar{\Delta}_{SR}^2(i\omega) &= \frac{-g^2}{4\beta} \int_0^\beta \sum_{<i,j>} < S_{i+}(\tau) S_{j-}(0) > e^{i\omega\tau} d\tau \\ &= \frac{-g^2}{4\beta} \sum_k (c_x + c_y) \chi_{+-}(k, i\omega) \simeq \frac{g^2}{2\beta} \sum_k \chi_{+-}(k, 0) \end{aligned} \quad (23)$$

which is equivalent to Eq. 22. (In the last equality in Eq. 23 the limit $i\omega \rightarrow 0$ is an adiabatic approximation²⁵, while the approximation is made that χ peaks near \vec{Q} .) Thus, *as long as there is short-range magnetic order (Δ or ρ_s non-zero), there will be a Mott (pseudo)gap*. Equation 23 was also derived by Schmalian, et al.⁶², but they did not discuss its significance.

C. Application to the Cuprates

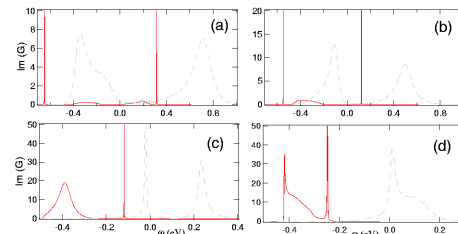


FIG. 17. Spectral functions for (a) $x = 0$, (b) $x = -0.04$, (c) $x = -0.10$, and (d) $x = -0.15$, at $T = 100K$. Solid lines at $(\pi, 0)$, and long dashed lines at $(\pi/2, \pi/2)$.

Using the correct $Im\Sigma^R$ from Eq. 19, and the calculated parameter values from Table I, ARPES spectra are calculated for electron-doped cuprates, at the four dopings for which detailed data are available¹⁰. Figure 17 shows typical calculated spectra for several \vec{k} -points in the a-b plane. Broadened Hubbard bands are found, which gradually smear out at high temperatures as δ increases (ξ decreases). There is a well defined pseudogap, with two peaks in the spectral function at a given \vec{k} . It should be stressed that since there is no interlayer coupling, long range antiferromagnetic order exists only at $T = 0K$. The resulting dispersions are shown in Fig. 18. Figures 19- 21 illustrate the temperature dependence of $Im(G)$ and $Im(\Sigma)$, for two dopings, $x = 0$ and -0.15 . The broadening of the peaks can be understood from Eq. 19: particle-hole excitations are present within a range $\pm\alpha_\omega/C$ of $\xi_{\vec{k}+\vec{Q}}$. Away from this particle-hole continuum the main peaks are sharp, while they broaden when they enter the continuum.

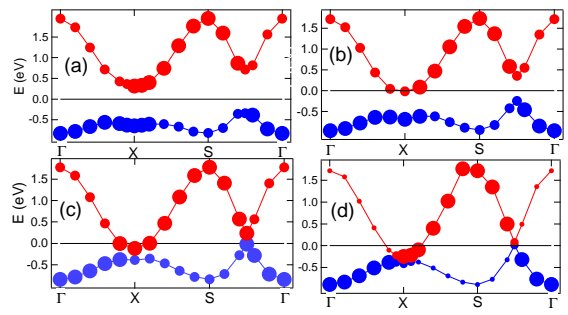


FIG. 18. Dispersion relations for electron doped materials, calculated at $T = 100K$: (a) $x = 0$ ($U/t = 6$), (b) $x = -0.04$ ($U/t = 5$), (c) $x = -0.10$ ($U/t = 3.5$), and (d) $x = -0.15$ ($U/t = 2.9$). Weaker features are denoted by smaller circles; for $x = -0.15$ all shadow features are extremely weak.

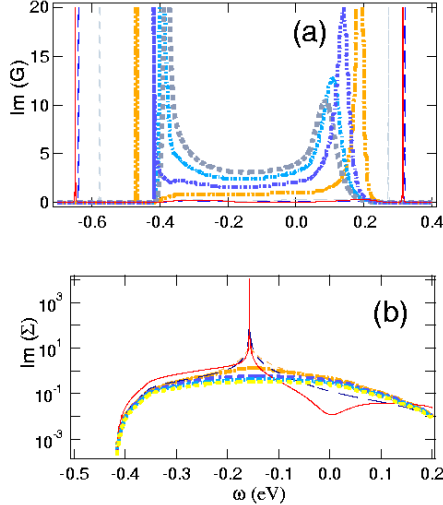


FIG. 19. Temperature dependence of (a) spectral function and (b) imaginary part of self energy, for $x = 0.0$ at $(\pi, 0)$. Temperatures are 100, 500, 1000, 2000, 3000, 4000, and 5000K.

Note that the Mott gap collapse is anisotropic: for the undoped case, the nodal gap collapses between 2–3000K, while a gap persists near $(\pi, 0)$ above 5000K. $\text{Im}(\Sigma)$ has striking oscillatory structure, particularly near $(\pi/2, \pi/2)$, which produces a similar weak structure in $\text{Im}(G)$ at low T. [Similar, weaker oscillations are present near $(\pi, 0)$, which can be better seen in Fig. 4c of Ref. 35.] In addition, there is a very intense, strongly T-dependent peak in $\text{Im}(\Sigma)$ exactly at $\xi_{\vec{k}+\vec{q}}$ (Fig. 19b – also present but not shown in Fig. 20b). It is the divergence of this peak as $T \rightarrow 0$ which signals the AFM transition. At low temperatures, the peak positions in $\text{Im}(G)$ have a temperature dependence consistent with the collapse of the Mott gap – e.g., the LHB shifts to higher energies (toward midgap) at higher temperatures. Some experiments on hole doped cuprates find the *opposite* dependence⁶³, which can possibly be understood as a localization or phase separation effect.

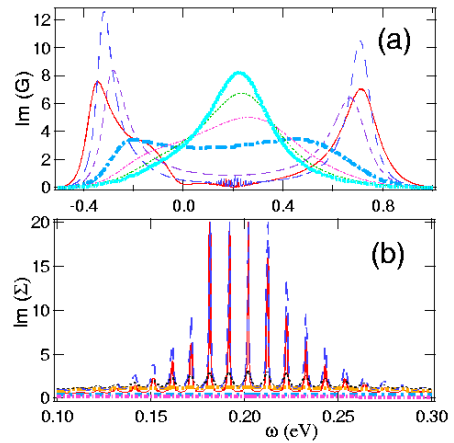


FIG. 20. Temperature dependence of (a) spectral function and (b) imaginary part of self energy, for $x = 0.0$ at $(\pi/2, \pi/2)$. Temperatures are 100, 500, 1000, 2000, 3000, 4000, and 5000K.

In contrast, for $x = -0.15$, Fig. 20, the splittings are absent near $(\pi/2, \pi/2)$, and vanish near $(\pi, 0)$ by ~ 500 K, and the lines actually *sharpen* on warming. If the effective U is reduced to $2.5t$, no splitting is found, but the peak position and broadening have an anomalous T dependence. Clearly, the system is very close to a QCP. Figure 22 shows in more detail how the spectrum evolves with U near this point.

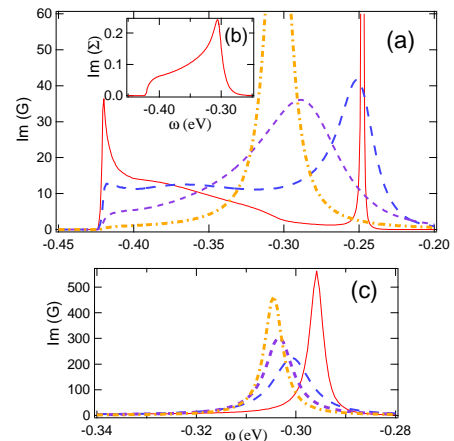


FIG. 21. Temperature dependence of spectral function for $x = -0.15$ at $(\pi, 0)$, for $U/t = 2.9$ (a) and 2.5 (c). Temperatures are 100 (solid line), 500 (long-dashed line), 1000 (short-dashed line), and 2000K (dot-dashed line). (b): imaginary part of self energy at $T = 100K$, $U/t = 2.9$.

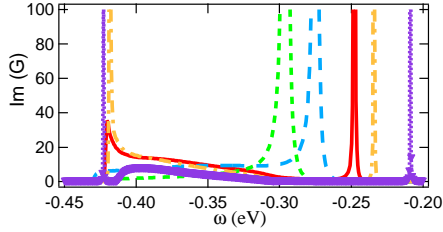


FIG. 22. U -dependence of spectral functions for $x = -0.15$ at $T = 100K$ near the $T = 0$ QCP, for $U/t = 2.5$ (short dashed line), 2.7 (long dashed line), 2.9 (solid line), 3.0 (dot-dashed line), and 3.2 (dotted line).

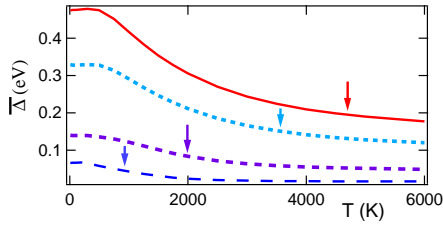


FIG. 23. Temperature dependence of gap $\bar{\Delta}$ for (from highest to lowest) $x = 0, -0.04, -0.10$, and -0.15 . Arrows show mean field transition temperature T_N .

Thus, the SCR calculation agrees with the mean-field results¹¹, if the mean-field gaps and transition temperatures are interpreted as the opening of a pseudogap at finite T , with the long-range AFM appearing only at $T=0$. A direct comparison of the transition temperatures is presented in Fig. 15d, presented on a linear T scale in Fig. 23. Moreover, the overall dispersions, Fig. 18 are in quite good agreement with the mean field results¹¹ and experiments¹⁰. This agreement is somewhat surprising, since the model is not fully self-consistent. For instance, the parameter C involves Landau damping of the spin waves by electron-hole excitations, and hence depends on the electronic dispersion near the Fermi level. Thus, the opening of the pseudogap should have a strong influence on C , which is not accounted for.

Finally, Fig. 24 displays Fermi surface map for $x = -0.04$ and -0.10 . The pseudogap along the zone diagonal associated with the hot-spot scattering⁶⁴ is clearly seen. These should be compared with the mean-field¹¹ and experimental¹⁰ results. One interesting aside: in the mean field calculation, with sharply defined bands, it was necessary to include a t'' parameter to reproduce the experimental hole pocket near the zone diagonal. In the SCR calculation the spectral function peaks are considerably broader, and no t'' parameter is needed.

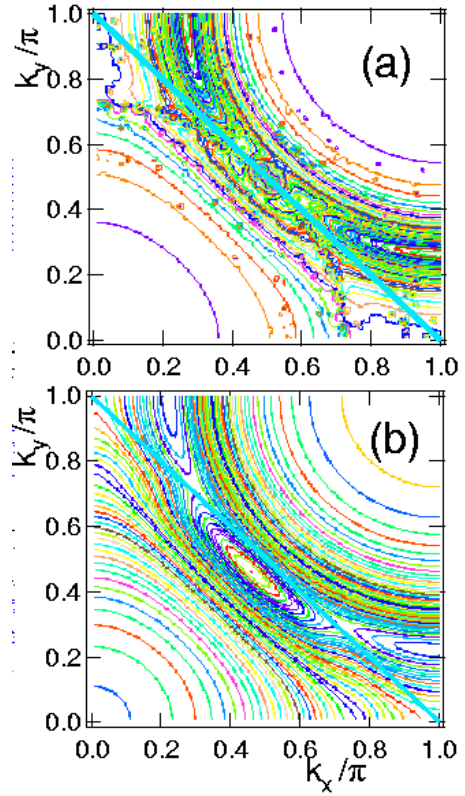


FIG. 24. Fermi surface map for $x = -0.04$ (a) and -0.10 (b).

V. THREE DIMENSIONAL NÉEL ORDER

In the physical cuprates, the interlayer hopping has an anomalous dispersion, generally written as $t_z = t_{z0}(c_x - c_y)^2$. This formula holds for bilayer splitting, and in general when the CuO_2 planes are stacked *uniformly*. However, as explained in Appendix E, many of the cuprates, including NCCO, have a *staggered layering*, with the Cu in one CuO_2 plane laying above a vacancy in the neighboring CuO_2 sheet. This leads to a *magnetic frustration*: the Cu in one sheet has four nearest neighbors in the adjacent sheet, two with spin up, two with spin down. This frustration is reflected in a more complicated dispersion of t_z :

$$t_z = t_{z0}(c_x - c_y)^2 \cos \frac{k_x a}{2} \cos \frac{k_y a}{2}, \quad (24)$$

which vanishes at $(\pi, 0)$ and $(0, \pi)$, and leads to a greatly reduced interlayer coupling. (Effects of AFM frustration associated with layering have been discussed in Ref. 65.)

The consequences of both uniform and staggered stacking are explored in Appendix E. If the c-axis resistivity is coherent, it can be used to estimate the interlayer hopping t_{z0} . It is found that the value of t_{z0} needed to produce a given resistivity anisotropy is approximately 5 times smaller for uniform stacking, to account for the

frustration in the staggered stacking. With the corresponding t_{z0} 's determined from resistivity, both forms of interlayer coupling give rise to comparable interlayer coupling, and hence a finite Néel temperature. While the optimal Q -vector depends on doping, at half filling both forms predict $\vec{Q} = (\pi, \pi, 0)$, consistent with experiment in La_2CuO_4 . Even for quite strong anisotropy, this mechanism can account for the observed T_{NS} (in fact, tends to overestimate T_N), without the necessity of invoking additional mechanisms, such as a Kosterlitz-Thouless transition, with the reduced spin dimensionality caused by spin-orbit coupling effects^{66–69}.

Within mode coupling theory⁷⁰ (Appendix E), the Néel temperature is found from the gap equation (Eqs. E1, C51)

$$\chi_0(T)U = \eta + \frac{3uTa^2 \ln(\frac{T}{T_{3D}})}{\pi A}, \quad (25)$$

where $T_{3D} \sim t_z^2$ is defined below Eq. E8. It is found that T_{3D} is approximately constant, independent of doping in the electron-doped regime. Apart from a small numerical factor, Eq. 25 differs from the isotropic three-dimensional result by the logarithmic factor, which diverges ($T_N \rightarrow 0$) as $t_z \rightarrow 0$.

Equation 25 can be rewritten in a suggestive form. Approximating ρ_s by $\rho_s^a = A(\chi_0 U - \eta)/12ua^2$ (Eq. C44), then, using Eq. 16, the Néel transition occurs when

$$J_z \left[\frac{\xi(T_N)}{\xi_0(T_N)} \right]^2 = \Gamma T_N \quad (26)$$

where $J_z = J(t_{z0}/t)^2$, $J = 4t^2/U$, and $\Gamma = 4t_{z0}^2/UT_{3D}$. A very similar form was proposed earlier⁷¹.

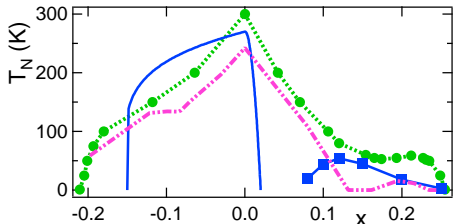


FIG. 25. Comparison of experimental Néel temperatures for NCCO and LSCO, (solid line), and for the stripe (magnetic) ordering transitions observed in Nd-substituted LSCO [52] (solid line with squares) with the model of interlayer coupling with staggered stacking and $t_{z0} = t/10 \sim 30\text{meV}$, plotted as $T_N/10$ (dot-dot-dash line). Also included is the approximate expression, Eq. 27 (dotted line with circles). (Note that there is a range of hole doping for which A is found to be negative; in this range T_N was arbitrarily assumed to vanish in the staggered model, $T_N = 0$.)

Figure 25 compares the calculated value of T_N with the experimental values. While the overall doping dependence is comparable, the calculated T_N is about an order of magnitude higher. The calculation is for staggered

stacking, with t_z adjusted to reproduce the observed resistivity anisotropy, but Appendix E shows that the overestimate is generic: the coefficient of the logarithm needs to be larger to reduce T_N . Also shown in Fig. 25 (dotted line) is a simplified model, which assumes that

$$T_0^* = \frac{\pi A}{3ua^2 \ln(\frac{T}{T_{3D}})} \quad (27)$$

is doping independent, $T_0^* = 1200K$. This model reproduces qualitatively the shape of the numerical calculation, but with a magnitude comparable to experiment. The magnitude of T_N could be matched almost quantitatively if U_{eff} also has a significant temperature dependence, as discussed in Appendix E . The overall doping dependence is also comparable to experiment. The agreement could be further improved by using a smaller value of t' , which would shrink the doping range over which Néel order occurs.

VI. DISCUSSION

A. Magnon Bose Condensation

Figure 26 shows the sharp peak which arises in $\text{Im}\Sigma$ at low T . The growth is exponential, approximately matching that of the coherence length, Eq. 16. (Note that it requires a fine mesh in the integral of Eq. 19 to capture this growth.) This peak arises exactly at the incipient magnetic zone boundary, and turns into true Bragg scattering at the transition to long range order: the increase in peak height is almost exactly compensated by a decrease in the width of the peak. A simple physical explanation is that the SDW transition can be interpreted as a *Bose condensation of the zone boundary magnons*. Then the Mermin-Wagner theorem reduces to the fact that in a two-dimensional system, Bose particles can only condense at $T = 0$. A similar explanation for the transition has been presented earlier³.

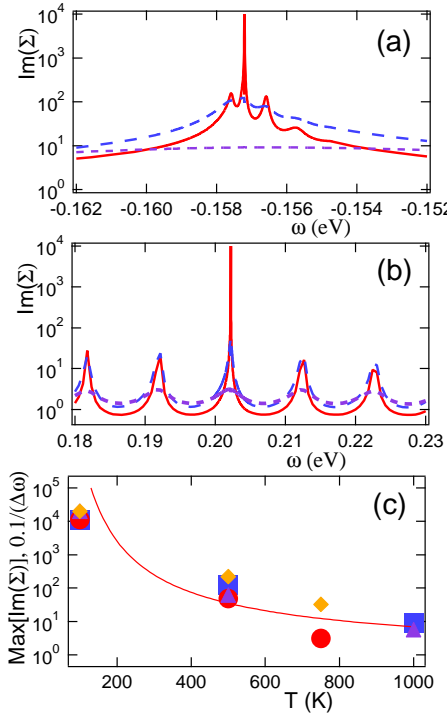


FIG. 26. (a,b): Blowups of $\text{Im}(\Sigma)$ for $x = 0$ at $(\pi, 0)$ (a) and $(\pi/2, \pi/2)$ (b) at $T = 100\text{K}$ (solid lines), 500K (long dashed lines), and 1000K (a) or 750K (b) (short dashed lines). (c) Maximum of $\text{Im}(\Sigma)$ vs T for $(\pi, 0)$ (squares) and $(\pi/2, \pi/2)$ (circles); $0.1/\text{full width at half maximum}$ for $(\pi, 0)$ (triangles) and $(\pi/2, \pi/2)$ (diamonds); solid line = corresponding $\xi(T)$, Eq. 16.

B. SCR Calculation of NAFL Parameters

The SCR is perhaps the simplest model in which fluctuation effects are included to satisfy the Mermin-Wagner theorem, allowing one to ask questions such as, how does a Mott gap appear if there is no long-range order to generate a smaller Brillouin zone? It can be seen that the Mott gap is really a pseudogap, and is relatively insensitive to the appearance of long-range Néel order. However, it must be kept in mind that the original SCR²⁵ is intended to describe *weak* itinerant ferromagnets and AFM's, and will have to be extended to account for the strong renormalization of the electronic bands.

Given these limitations, the present paper attempts to use the SCR to calculate the parameters, A , C , etc., for an NAFL-like model of the low energy physics. The principal findings include:

- the program *fails* for hole doped cuprates, since the parameter A is negative, signalling an instability of the commensurate AFM phase against either incommensurate SDW phases or nanoscale phase separation.
- For electron doped cuprates, considerable progress can be made, but the model still has problems, in particular a poorly defined spin-wave interaction parameter u .

Here u is estimated by comparison with sigma model results near half filling, but its possible doping dependence is unknown.

- The present theory differs from conventional NAFL theory by the inclusion of two cutoff parameters, q_c and ω_c^- . These cutoffs shrink to zero at either the H- or C-points, and in particular cause the A parameter to have a strong temperature dependence in the electron-doping regime.

- The combined SCR and mean-field¹¹ results are in excellent agreement with the ARPES data¹⁰ on the doping dependence of the Mott transition in the electron-doped cuprates.

- While the collapse of the Mott gap and the termination of the hot spot regime are in principle independent QCPs, in practice they fall very close to each other. The present calculations and Ref. 20 explain why this is so.

These points are discussed in more detail in the following subsections.

C. Mott Transition vs Slater Antiferromagnetism

In reviewing the history of magnetism, Anderson recently pointed out⁷² that the theories fall into two diametrically opposed classes: band theory and atomic models, and the latter are typically more successful. In particular, for strongly correlated Mott insulators Mott's model of nearly localized spins seems like a better starting point than Slater's theory of spin density wave antiferromagnetism. The main problem is that the Slater theory ties the Mott gap to antiferromagnetic order, predicting too high a Néel temperature.

While a localized picture may be a more convenient starting point near half filling, nevertheless it should be possible to develop a (perhaps more complicated) picture based on band theory. There is a general desideratum to be able to extend band structure calculations to all materials; moreover, this is important in the present instance because the doping dependence of U suggests that there is a crossover from strong to intermediate correlations, which may be better handled by working throughout in a band structure formalism. The present mode coupling calculation seems to be an appropriate starting point. The Mermin-Wagner theorem leads to a decoupling of the Mott gap and Néel order. How this might be extended to three-dimensional Mott insulators remains unclear.

Local physics should show up in a band structure calculation as a very narrow band width. In a mean field SDW calculation, the width of the Hubbard bands, $\sim t^2/U \sim J$, is not small.

D. Stoner Criterion and Crossover from Small to Large FS

In the Hartree-Fock model, the crossover from small to large Fermi surface is *coincident* with Mott gap collapse, and comparison with experiment suggests that this correctly describes the situation in electron doped NCCO. The SCR theory confirms this result and offers additional insights. Fluctuations preclude long-range order at finite temperatures (in the absence of interlayer coupling), so the physics is that of a *zero temperature* AFM *QCP*, controlled by a Stoner criterion: the QCP occurs when χU is too small. At finite temperatures, the Mott gap is replaced by a pseudogap, and the FS crossover still coincides with the collapse of the Mott pseudogap, which occurs at the QCP. Whether a similar crossover can occur in the absence of Mott gap collapse remains to be seen.

E. Hole Doped Cuprates

The present calculations make two predictions for hole-doped cuprates: (1) there are strong indications for instability against phase separation and stripe physics; but (2) despite this, the termination of strong magnetic fluctuations should be approximately electron-hole symmetric²⁰ – associated with the symmetric susceptibility plateau in Fig. 1a.

1. Stripes

The situation in hole doped cuprates is complicated by the presence of stripes. At all levels, mean-field, RPA, SCR, striking differences between hole and electron doping are clearly revealed. All techniques provide strong evidence for the instability of the AFM state for hole doping, while it remains stable under electron doping. In earlier Hartree-Fock and RPA calculations, evidence for the instability of the hole doped phase was found *in the ordered magnetic phase*, within the smaller magnetic Brillouin zone: e.g., the spin wave dispersion is unstable. In the SCR approach, there is no phase transition at finite temperatures, but *even in the paramagnetic phase* there is evidence for the instability. A detailed analysis of the real part of the bare susceptibility (as appropriate for a Stoner criterion) provides evidence for instability of a commensurate magnetic phase at \vec{Q} (negative curvature A).

2. Pseudogap

In hole doped cuprates, ARPES finds two features which are commonly referred to as pseudogaps – a ‘hump’ feature found near $(\pi, 0)$ at higher binding energy than

the main, superconducting ‘peak’, and the ‘leading edge gap’, a loss of spectral weight in the immediate vicinity of the Fermi level. This latter feature is not explained by the present calculation; it may be associated with the onset of strong superconducting fluctuations^{62,73}. Alternatively, such a gap has been found in a dynamical cluster expansion calculation of the Hubbard model⁷⁴.

On the other hand, the ‘hump’ feature can be consistently interpreted as the collapse of the Mott pseudogap^{62,20}. While ARPES only sees the feature below the Fermi level associated with the lower Hubbard band (LHB), tunneling^{73,75,76} finds an approximately symmetrical peak feature above the Fermi level, associated with the UHB – as if the pseudogap were pinned to the Fermi level. This has led to a number of alternative models for the pseudogap, in terms of superconducting or charge density wave (CDW) fluctuations (the latter possibly related to stripe physics). Recently²⁰ it was found that the same mean field model of Mott gap collapse can approximately explain the data (see Fig. 2b). In this model, the lower pseudogap peak is the VHS of the LHB, while the upper peak is due to the leading edge of the UHB. As the Mott gap collapses, the two features merge. A careful tunneling study of the ‘hump’ features could look for the predicted asymmetry of the features about the Fermi level. Such a study should best be done in single layer $\text{Bi}_2\text{Sr}_2\text{CuO}_6$,⁷⁷ where complications due to bilayer splitting are absent.

The above interpretation requires that for hole doping also the Mott gap must collapse slightly above optimal doping. This is consistent with recent experimental observations of a QCP²¹. The early SCR results of Table II point in the same direction: the very small and positive values found for the Stoner parameter y_0 in optimally and overdoped cuprates suggests the proximity to a QCP near optimal doping. Moreover, the model predicts that at the QCP, where the pseudogap just closes, the Fermi level is *exactly at the VHS* (H-point). This result had been found experimentally in some lightly overdoped cuprates^{78,79}.

While the doping of Mott gap collapse is approximately electron-hole symmetric, some significant differences remain. Thus, for electron doping the magnetic correlation length remains large up to the QCP, while the correlation length is only a few lattice constants on the hole doped side. This may be related to competing order – indeed, in Nd substituted LSCO, long-range incommensurate magnetic order is found⁷ up to $x = 0.2$. Alternatively, Schmalian, et al.⁶² were able to reproduce a hump-like pseudogap with small correlation length, by a careful summation of the full diagrammatic perturbation series. [Note that near a VHS, all competing electron-hole instabilities – SDW, CDW, flux phase, shear (‘Pomeranchuk’) instability – will lead to similar pseudogaps near $(\pi, 0)$, and indeed in the presence of strong fluctuations, all will contribute in a comparable fashion, $\Delta^{*2} \sim \sum_i \Delta_i^2$.]

F. VHS

1. Electron-Hole Asymmetry

To study the role of the VHS in the Mott transition and high- T_c superconductivity, one would ideally like to study a system in which one could turn the VHS on or off. Electron vs hole doping of the cuprates would appear to approach this ideal. In switching from electron to hole doping (from NCCO to LSCO) T_c increases by less than a factor of two, and apparently remains d-wave, while the normal state properties change drastically, with nanoscale phase separation on the hole doped side only.

On the other hand, the one hole vs one electron systems should be much more similar: in either case, nearest neighbor hopping is frustrated by breaking local antiferromagnetic order. Hence in both cases, the low energy states will be magnetic polarons. Indeed, the electron-doped polarons may be more localized, since there is no inter polaron attraction (i.e., tendency to phase separation). The ARPES spectra for low-electron doping ($x=0.04$) show an additional pseudogap at the Fermi level, which may be related to localization.

2. Temperature Dependent VHS

As noted by Onufrieva and Pfeuty⁵⁰, the VHSs associated with the susceptibilities (and hence with charge or spin nesting) are *different* from those associated with the density of states (and superconductivity). Thus, whereas superconductivity will occur at the same optimal doping for all temperatures, the doping of maximal nesting instability *is a strong function of temperature*.

This contrasting behavior of nesting vs pairing *susceptibilities* is related to a characteristic difference in the nature of the two *instabilities*. A superconducting instability has an intrinsic electron-hole symmetry, which means that the gap is tied to the Fermi level, and a full (s- or d- wave) gap can be opened at any doping level. On the other hand, a nesting gap is dispersive, and only part of it lies at the Fermi level (except in special cases). Furthermore, a (superlattice) Luttinger's theorem must be obeyed, requiring the presence of residual Fermi surface pockets. Stated differently, a full nesting gap can only open at integer filling, so *as the interaction strength increases, any nesting instability must migrate to integral doping* (e.g., half filling in the original band structure). This same VHS migration is mirrored in the T-dependence of the magnetic (or charge) susceptibility.

3. VHS Transitions

We have seen that the doping-dependent U_{eff} gives rise to a Mott gap collapse near the edges of the susceptibility plateau in Fig. 1. If U_{eff} is smaller (dot-dashed

line: U_{eff} reduced by 2/3), more complicated behavior should arise. Due to the peak in χ near the H-point, there could be a reentrant transition, with one magnetic order near half filling, and a second near the VHS. For an even smaller U_{eff} (or replacing $U_{eff} \rightarrow J$)⁵⁰, the transition near $x = 0$ can be eliminated, leaving a spin density wave transition near the VHS. In principle there could even be a phase separation *between two AFM phases*: an insulating phase near half filling and a metallic phase near the VHS.

G. Future Directions

It must be stressed, however, that the present theory is not fully self-contained. There are three significant limitations. First, an improved calculation of the doping dependence of the Hubbard U parameter is a desideratum, perhaps along the lines of earlier calculations^{80,81,61}. Since all of these calculations lead to different doping dependences for $U(x)$, the actual doping dependence must be regarded as an unresolved issue.

Second, several unsuccessful attempts have been made to calculate the quartic interaction parameter u . A simple *ansatz* for $u(x)$ is introduced, based on consistency with the $t - J$ model, which leads to good results. A deeper understanding of why this works, and whether u is doping dependent, is desirable.

Finally, the susceptibility was calculated with the bare electronic bands, but when the bands are renormalized to first order in χ a pseudogap opens. This gap should be self consistently incorporated into the calculation of χ , as in the FLEX and spin fermion approaches; it is expected to have a profound effect on the temperature dependence of the parameters (especially A) and on the residual density of states in the pseudogap, particularly near $x = 0$.

VII. CONCLUSIONS

The main results of this rather long paper are briefly summarized:

- Fluctuation effects were added to the mean field Hubbard model via a mode coupling calculation, which allowed satisfying of the Mermin-Wagner theorem ($T_N = 0$). It was found that the mean-field gap Δ_{mf} and Néel temperature T_N^{mf} evolved into a pseudogap $\Delta_{ps} \sim \Delta_{mf}$ and an onset temperature $T^* \sim T_N^{mf}$ (as is familiar from the related CDW results).
- The resulting dispersions and Fermi surfaces are in excellent agreement with photoemission experiments on electron-doped cuprates¹⁰, while the pseudogap seems consistent with ARPES and tunneling results in hole doped cuprates²⁰. It is interesting to note that a recent $t - t' - t'' - J$ model calculation seems consistent with the first doped carriers forming weakly interacting

quasiparticles in pockets of the respective upper or lower Hubbard bands, for either electron or hole doping⁸².

- The zero-temperature Néel transition is controlled by a Stoner-like criterion, hence is sensitive to the bare susceptibility and in turn to the Fermi surface geometry (hot spots). This lead to an approximately electron-hole symmetric QCP near optimal doping (termination of hot spot regime), at which both zero temperature Néel transition and pseudogap transition simultaneously terminate.
- The model leads to a NAFL-type susceptibility, and the calculation of the NAFL parameters has been reduced to a calculation of the coupling parameters U and u , the former having a significant doping (and possibly temperature) dependence. At present, $U(x)$ is estimated from experiment, and the mode coupling u via consistency with the $t - J$ model. (A small portion of the renormalization of U arises from quantum corrections to the Stoner criterion.)
- Whereas the antiferromagnetic state at \vec{Q} is stable to electron doping, hole doping leads to an incommensurability, which is interpreted as an indication of instability to phase separation (as found in the mean field calculations). This asymmetry follows from the properties of the VHS.
- Finally, a striking *temperature/frequency dependence* of the susceptibility peak, from the VHS at low T to half filling at high T , found earlier⁵⁰, is interpreted in terms of Luttinger's theorem: if the coupling is strong enough to open a full gap, the gap must fall at half filling.

Acknowledgments: Part of this work was done while I was on sabbatical at the Instituto de Ciencia de Materiales de Madrid, CSIC, Cantoblanco, E-28049 Madrid, Spain, supported by the Spanish Ministerio de Educación through grant SAB2000-0034. I thank my hosts, María Vozmediano and Paco Guinea, for a very stimulating visit, for numerous discussions, and for correcting an error in the original calculation.

I thank Walter Harrison for stimulating conversations on calculating the interlayer coupling.

APPENDIX A: THREE BAND MODEL

A major simplification of the present calculation is to treat the cuprates in a one-band model. This is consistent with the Zhang-Rice picture⁸³, although the approximation is less drastic for electron doping, since the upper Hubbard band is already predominantly copper-like. Nevertheless, the model also describes the doping dependence of the ‘lower Hubbard band’, which is really a charge transfer, predominantly oxygen-like band. Here an explanation for why this simplification works is suggested.

Even without carrying out self-consistent calculations, the nature of the Mott transition can be understood by introducing a doping dependent gap. The energy bands can be calculated from the hamiltonian matrix

$$H = \sum_j \Delta d_j^\dagger d_j + \sum_{\langle i,j \rangle} t_{CuO} [d_j^\dagger p_i + (c.c.)] + \sum_{\langle j,j' \rangle} t_{OO} [p_j^\dagger p_{j'} + (c.c.)] \quad (A1)$$

where Δ is the difference in on-site energy between copper and oxygen, t_{CuO} is the copper-oxygen hopping parameter, and t_{OO} the oxygen-oxygen hopping parameter. For good agreement with the doping dependence of the one band model, it is necessary to properly incorporate the Hartree correction to the self energy, $\Delta = \Delta_0 + \Sigma_H$, $\Sigma_H = Un_\downarrow$ (for up spins), and $n_\downarrow = n/2 - m_Q$, with n the average electron energy. In Figs. 27, $\Delta_0 = 0$ is assumed.

The band dispersion is extremely similar to that found in the one band model, Fig. 3 of Ref. 11, even though the lower band crosses over from the Zhang-Rice (hybridized copper-oxygen band) at half filling to a more copper like lower Hubbard band with increasing electron doping. In addition, the effective magnetizations are proportional (inset, Fig. 27d), although the one-band model overestimates the magnetization by 1/3. This can be understood: in the three-band model, the shape of the Hubbard bands is fixed by the combined effects of the magnetic instability and hybridization with the oxygen band. In the one band model, only the former effect is present, necessitating a larger value of m to produce the same net splitting.

This remarkable agreement between one and three-band models goes well beyond the Zhang-Rice model. That model is restricted to the LHB in a small range of doping near half filling; the present results compare both LHB and UHB over the full range of electron doping. The result is nontrivial – in the three band model, the bonding and non-bonding bands are also split into upper and lower Hubbard bands. This degree of agreement comes about because the parameter Δ is approximated by the two components (magnetic and nonmagnetic) of the Hartree term. In turn, this suggests that in the absence of magnetic effects the Cu and O energies are nearly degenerate – as found in early LDA band structure calculations (see discussion in Ref. 84).

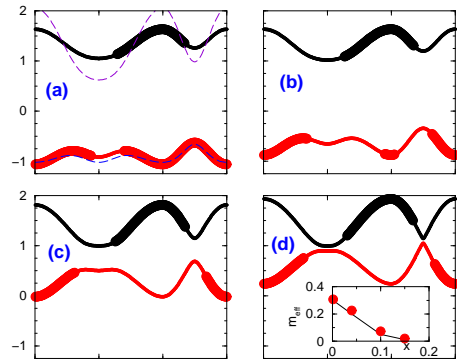


FIG. 27. Dispersion of two antibonding bands in three-band model, assuming $m_Q = 0.3$ (a), 0.2 (b), 0.05 (c), and 0.01 (d). Inset to d: effective magnetization $m_{eff} = mU/6t$ for the three-band (solid line) and one-band (filled circles) models. The one-band result has been multiplied by 3/4 to better agree with the three-band results.

APPENDIX B: CHARGE SUSCEPTIBILITY AND U_{eff}

The proper choice of vertex corrections is an unresolved issue in the analysis of the Hubbard model. It is known to be of critical importance for generating a pseudogap⁸⁵. Here, by comparing simple mean-field and SCR models to experiment, it is shown that the net effect of vertex corrections is to make the coupling U effectively doping (and possibly temperature) dependent. Kanamori⁴⁶ showed that the effective Hubbard U should decrease with doping, as an electron can hop around, and hence avoid, a second electron. In the limit of a nearly empty (or full) band, this should lead to a correction of the form $U_{eff} \sim U/(1 + U/W)$, where $W = 8t$ is the bandwidth. It was found^{81,61} that Monte Carlo calculations of the susceptibility of a doped Mott insulator were approximately equal to the RPA susceptibility with suitable U_{eff} , and Chen, et al.⁸¹ suggested the explicit form $U_{eff} = U/(1 + \langle P \rangle U)$, with P given by a vertex correction to the susceptibility and $\langle \dots \rangle$ an average over \vec{q} , at zero frequency. Figure 28b presents a calculation for U_{eff} based on Chen, et al. However, whereas Chen, et al. performed the average in the paramagnetic phase, using bare Green's functions, here the dressed Green's functions appropriate to the Néel phase are used, to approximately incorporate the effect of this gap. This makes little difference, since P is dominated by the intraband terms, and hence remains finite at half filling. Explicitly,

$$P = -\frac{1}{N} \sum_{i,j,k} \hat{U}_{i,j}(k, k+q) \tilde{F}_{i,j}(k, k+q), \quad (B1)$$

$$\tilde{F}_{i,j}(k, k') = \frac{1 - f_k^i - f_{k'}^j}{E_i(\vec{k}) + E_j(\vec{k}') - \omega - i\delta}, \quad (B2)$$

$$E_{\pm}(\vec{k}) = \frac{1}{2}(\epsilon_k + \epsilon_{k+q} \pm E_0), \quad (B3)$$

$$E_0 = \sqrt{(\epsilon_k - \epsilon_{k+q})^2 + 4\Delta^2}, \quad (B4)$$

$$\hat{U}_{i,j}(k, k') = \frac{1}{4}(1 + iA_k)(1 + jA_{k'}) + ijB_k B_{k'}, \quad (B5)$$

with i, j summed over $+, -$, Δ the AFM gap, and $A_k = (\epsilon_k - \epsilon_{k+Q})/E_{0k}$, $B_k = \Delta/E_{0k}$. In agreement with Chen,

et al., the calculation finds U to be renormalized by a factor of 2 at finite doping, but does not recover a large U near half filling, although different results are found depending on whether $x = 0$ from the start (triangle) or whether $x \rightarrow 0$ from the hole or electron doping sides.

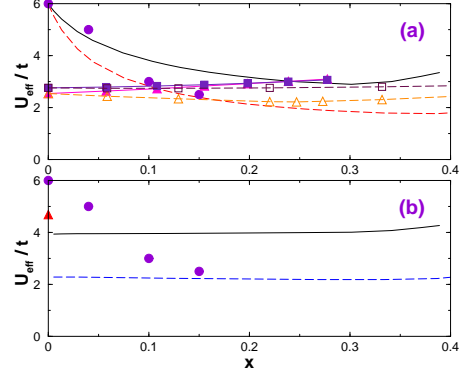


FIG. 28. Calculated U_{eff} assuming (a) simple screening or (b) full vertex correction of Chen, et al. [81]. In both cases, a bare $U = 6.75t$ was assumed. Solid lines = electron doping; long dashed lines = hole doping; triangles (squares) in a = paramagnetic screening of U , at $T = 1K$ ($2000K$); triangle in b = undoped; circles = data of Ref. [10].

For modelling purposes, it is useful to have a U_{eff} which evolves smoothly from a large value at half filling to a reduced, Kanemori value at finite doping. A simple toy model consists of taking the RPA screening of a charge response. There should be a close connection between the Kanemori mechanism and screening. Screening involves creation of a correlation hole about a given charge, while Kanemori's U_{eff} involves the ability of a second charge to move around the first, while avoiding double occupancy. Near half filling, the second charge must move in the correlation hole. Approximating¹¹ the vertex correction by the RPA screening of the charge susceptibility,

$$U_{eff} = \frac{U}{1 + \langle \chi \rangle U}, \quad (B6)$$

it is possible to reproduce¹¹ the experimentally observed¹⁰ doping dependence, while matching the calculation of Chen, et al. away from half filling, Fig. 28a.

In this calculation, issues of self-consistency are also important. To minimize screening at half filling, it is necessary to reproduce the gap in the susceptibility. Hence, the susceptibility in Eq. B6 is approximated by the charge susceptibility in the AFM state, χ_0^{00} from Eq. 2.24 of Ref. 1, evaluated with the bare $U = 6.75t$. (In principle, at finite doping there is a coupling to the longitudinal magnetic susceptibility¹⁶, but this is neglected for simplicity.) The importance of using the AFM susceptibility is illustrated in Fig. 28a: the solid and dashed lines show U_{eff} calculated using the charge susceptibility in the Néel state, while the corresponding lines with triangles use the paramagnetic susceptibility at low T .

The latter calculation finds a nearly doping independent, but small U_{eff} ; the former reproduces a large, weakly screened U near half filling. Such a difference is expected in terms of screening: when there is no gap at half filling, the enhanced susceptibility should be better able to screen U , resulting in a smaller U_{eff} . This suggests that U_{eff} should have an important *temperature dependence* as the gap decreases – which in turn will cause the gap to close at a lower temperature. Figure 28a also shows that there is a weak temperature dependence of the screening. The calculations suggest that the large values of U found in the cuprates are characteristic mainly of the half filled regime and relatively low temperatures. A similar but larger screening effect was recently reported by Esirgen, et al.⁸⁰.

This procedure is still not fully self consistent. If there is a large difference between the bare U and the screened U_{eff} , the gap in χ should depend on the actual U_{eff} . However, since $U_{eff} \simeq U$ at half filling, any simple improvement will not significantly change the overall doping dependence. This is the same kind of lack of self-consistency found for the SCR approach, and will be here neglected.

APPENDIX C: PATH INTEGRAL CALCULATION

1. Formalism

The partition function of the Hubbard model can be written as a path integral⁴⁵:

$$Z = \int DC^\dagger DC \exp \left[- \int_0^\beta d\tau L \right], \quad (C1)$$

with Lagrangian

$$L = \sum_{i,\sigma} C_{i\sigma}^\dagger (\partial_\tau - \mu) C_{i\sigma} - \sum_{i,j,\sigma} C_{i\sigma}^\dagger t_{i,j} C_{j\sigma} + U \sum_i n_{i\uparrow} n_{i\downarrow}. \quad (C2)$$

The quartic term can be decoupled by a Hubbard-Stratonovich transformation

$$Z = \int D\phi DC^\dagger DC \exp \left[- \int_0^\beta d\tau L(\phi, C^\dagger, C) \right], \quad (C3)$$

$$L(\phi, C^\dagger, C) = \sum_{i,\sigma} C_{i\sigma}^\dagger (\partial_\tau - \mu) C_{i\sigma} - \sum_{i,j,\sigma} C_{i\sigma}^\dagger t_{i,j} C_{j\sigma} + \frac{U}{4} \sum_i \phi_i^2 + \frac{U}{2} \sum_i \phi_i (n_{i\uparrow} - n_{i\downarrow}) \quad (C4)$$

(neglecting a term involving $n_{i\uparrow} + n_{i\downarrow}$). Integrating out the Fermion fields leaves an effective action in the field ϕ :

$$Z = \int D\phi e^{-S_{eff}}, \quad (C5)$$

$$-S_{eff} = \frac{U}{4} \int_0^\beta d\tau \sum_i [\phi_i^2 - \text{Tr} \ln(\partial_\tau - \mu - t_{i,j} + \sigma \frac{U}{2} \phi_i)]. \quad (C6)$$

Fourier transforming in space and (imaginary) time, the trace term can be rewritten

$$\text{Tr} \ln(-G_0^{-1} + V) = \text{Tr} \ln(-G_0^{-1}) - \sum_{n=1}^{\infty} \frac{1}{n} \text{Tr}(G_0 V)^n, \quad (C7)$$

with

$$G_0(\vec{k}, i\omega_n) = \frac{\delta_{\sigma,\sigma'} \delta_{n,m} \delta_{\vec{k},\vec{k}'}}{i\omega_n - \xi_{\vec{k}}}, \quad (C8)$$

$$V = \frac{\delta_{\sigma,\sigma'}}{\sqrt{\beta N_0}} \frac{\sigma U}{2} \phi(\vec{k} - \vec{k}', i\omega_n - i\omega_m), \quad (C9)$$

with $\xi_{\vec{k}} = \epsilon_{\vec{k}} - \mu$. In Eq.C7, the odd terms in n average to zero, so expanding the action to fourth order in ϕ yields

$$S = \frac{1}{2} \sum_{\vec{q}, i\omega_n} \Pi_2(\vec{q}, i\omega_n) \phi(\vec{q}, i\omega_n) \phi(-\vec{q}, -i\omega_n) + \frac{1}{4(\beta N_0)^2} \sum' \Pi_4(\vec{q}_i, i\omega_i) \phi(\vec{q}_1, i\omega_1) \phi(\vec{q}_2, i\omega_2) \times \phi(\vec{q}_3, i\omega_3) \phi(\vec{q}_4, i\omega_4), \quad (C10)$$

where the prime in the second sum means summing over all \vec{q}_i, ω_i , such that $\sum_{i=1}^4 \vec{q}_i = 0$, $\sum_{i=1}^4 \omega_i = 0$,

$$\Pi_2(\vec{q}, i\omega_n) = \frac{U}{2} [1 - U \chi_0(\vec{q}, i\omega_n)], \quad (C11)$$

$$\Pi_4(\vec{q}, i\omega_n) = \frac{U^4}{8} \sum_{\vec{k}, i\epsilon_n} G_0(\vec{k}, i\epsilon_n) G_0(\vec{k} + \vec{q}_1, i\epsilon_n + i\omega_1) \times G_0(\vec{k} + \vec{q}_1 + \vec{q}_2, i\epsilon_n + i\omega_1 + i\omega_2) G_0(\vec{k} - \vec{q}_4, i\epsilon_n - i\omega_4), \quad (C12)$$

and χ_0 is the dynamic susceptibility

$$\chi_0(\vec{q}, i\omega_n) = \frac{-1}{\beta N_0} \sum_{\vec{k}, i\epsilon_n} G_0(\vec{k}, i\epsilon_n) G_0(\vec{k} + \vec{q}, i\epsilon_n + i\omega_n) = \frac{1}{N_0} \sum_{\vec{k}} \frac{f(\xi_{\vec{k}+\vec{q}}) - f(\xi_{\vec{k}})}{i\omega_n + \xi_{\vec{k}} - \xi_{\vec{k}+\vec{q}}}. \quad (C13)$$

The mean field solution corresponds to assuming $\phi_i = \phi_0 e^{i\vec{Q} \cdot \vec{R}_i}$ and finding the saddle point solution of Eq. C6. Including interactions by summing bubble or ladder diagrams¹ leads to the RPA susceptibility (see

Eq. C14 below), from which the spin wave spectra are calculated¹³. Fluctuations about the mean field solution are described by Eq. C10. Due to the Mermin-Wagner theorem, these fluctuations are in the high temperature limit $T > T_N$. A naive perturbational analysis diverges (as demonstrated below), so a self-consistent analysis is necessary. Following the self-consistent renormalization (SCR) model of Moriya^{25,26}, the exact dynamical susceptibility can be written as

$$\chi(\vec{q}, i\omega_n) = \frac{\chi_0(\vec{q}, i\omega_n)}{1 - U\chi_0(\vec{q}, i\omega_n) + \lambda_U(\vec{q}, i\omega_n)}, \quad (\text{C14})$$

with the RPA susceptibility given by Eq. C14 with $\lambda_U = 0$.

Solving Eq. C14 requires an equation for λ_U . An approximate solution is found by replacing $\lambda_U(\vec{q}, i\omega_n)$ by a constant

$$\lambda \equiv \lambda_U(0, 0) = \chi_0 \left(\frac{\partial^2 \Delta F(M, T)}{\partial M^2} \right)_{M=0}, \quad (\text{C15})$$

where the total free energy is written as $F(M, T) = F_{HF}(M, T) + \Delta F(M, T)$, with F_{HF} the Hartree-Fock free energy and

$$\begin{aligned} \Delta F(M, T) &= -T \sum_{\vec{q}, n} \int_0^U dU [\chi(\vec{q}, i\omega_n) - \chi_0(\vec{q}, i\omega_n)] \\ &= T \sum_{\vec{q}, n} [\ln(1 - U\chi_0(\vec{q}, i\omega_n) + \lambda) + U\chi_0(\vec{q}, i\omega_n)]. \end{aligned} \quad (\text{C16})$$

Equation C16 can be solved by expanding about the expected ordered state. The ordered states are found from the zeroes of the denominator of the dynamical susceptibility, Eq. C14. For the present case, the largest bare susceptibility corresponds to antiferromagnetic order, $\vec{q} = \vec{Q}$. Then, defining

$$\delta = 1 - U\chi_0(\vec{Q}, 0) + \lambda, \quad (\text{C17})$$

and $\delta_0 = \delta - \lambda$, it will be shown that $\delta \geq 0$, and $\delta \rightarrow 0$ as $T \rightarrow 0$ – that is, there is no finite temperature phase transition (the Mermin-Wagner theorem is satisfied).

2. SCR Analysis

Following the conventional analysis, Eq. C16 is expanded in terms of the small parameters ω and $\vec{q}' \equiv \vec{q} - \vec{Q}$ (analytically continuing $i\omega_n \rightarrow \omega + i\epsilon$):

$$1 - U\chi_0(\vec{q}, \omega) + \lambda = \delta + Aq'^2 - B\omega^2 - iC\omega, \quad (\text{C18})$$

where the expansion coefficients are

$$A = -Ua^2 \sum_{\vec{k}} \left[\frac{f'(\epsilon_{\vec{k}})}{(\epsilon_{\vec{k}+\vec{Q}} - \epsilon_{\vec{k}})^2} + \frac{f(\epsilon_{\vec{k}}) - f(\epsilon_{\vec{k}+\vec{Q}})}{(\epsilon_{\vec{k}+\vec{Q}} - \epsilon_{\vec{k}})^3} \right], \quad (\text{C19})$$

$$\begin{aligned} A &= \frac{Ua^2}{2} \sum_{\vec{k}} \left[\left(\frac{f(\epsilon_{\vec{k}}) - f(\epsilon_{\vec{k}+\vec{Q}})}{(\epsilon_{\vec{k}+\vec{Q}} - \epsilon_{\vec{k}})} \right) \left(\frac{1}{8} + \frac{32t'c_y^2s_x^2}{(\epsilon_{\vec{k}+\vec{Q}} - \epsilon_{\vec{k}})^2} \right) \right. \\ &\quad \left. - f'(\epsilon_{\vec{k}}) \left(\frac{1}{16} + \frac{2t'}{(\epsilon_{\vec{k}+\vec{Q}} - \epsilon_{\vec{k}})} + \frac{32t'^2c_y^2s_x^2}{(\epsilon_{\vec{k}+\vec{Q}} - \epsilon_{\vec{k}})^2} \right) \right. \\ &\quad \left. - f''(\epsilon_{\vec{k}}) \left(t'(1 - c_x c_y) + \frac{2s_x^2(t^2 + 4t'^2c_y^2)}{(\epsilon_{\vec{k}+\vec{Q}} - \epsilon_{\vec{k}})} \right) \right], \end{aligned} \quad (\text{C20})$$

$$B = U \sum_{\vec{k}} \left[\frac{f(\epsilon_{\vec{k}}) - f(\epsilon_{\vec{k}+\vec{Q}})}{(\epsilon_{\vec{k}+\vec{Q}} - \epsilon_{\vec{k}})^3} \right], \quad (\text{C21})$$

$$C = -2\pi U \sum_{\vec{k}} [f'(\epsilon_{\vec{k}}) \delta(\epsilon_{\vec{k}+\vec{Q}} - \epsilon_{\vec{k}})]. \quad (\text{C22})$$

These are similar to results found previously²⁶, specialized to the dispersion of Eq. 1. However, with this dispersion the A and B integrals formally diverge. Hence a more careful analysis is needed, presented in Appendix D. For now, A , B , and C will be treated as parameters.

a. Free Energy

Here, λ is determined by minimizing the free energy, including quartic, Π_4 , corrections⁴⁵. With the variational estimate

$$F = F_0 + \frac{1}{\beta} \langle S - S_0 \rangle_{S_0}, \quad (\text{C23})$$

the action S (Eq. C10) becomes

$$\begin{aligned} S &= \frac{U}{4} \sum_{\vec{q}, i\omega_n} (\delta_0 + Aq'^2 + C|\omega_n|) \phi(\vec{q}, i\omega_n) \phi(-\vec{q}, -i\omega_n) \\ &\quad + \tilde{u} \int_0^\beta d\tau \int d^2\vec{r} [\phi(\vec{r}, \tau)]^4, \end{aligned} \quad (\text{C24})$$

and S_0 is given by the same equation, with δ_0 replaced by the variational parameter δ . Here $\tilde{u} = \Pi_4 a^d / 4\beta N_0$, with $d = 2$ and Π_4 evaluated at $\vec{q}_i = (0, \vec{Q}, 0, -\vec{Q})$, $\omega_i = 0$, since higher order corrections are irrelevant. Then to Gaussian order

$$\begin{aligned} \langle S - S_0 \rangle_{S_0} &= \frac{U}{4} \sum_{\vec{q}, i\omega_n} (\delta_0 - \delta) \langle \phi(\vec{q}, i\omega_n) \phi(-\vec{q}, -i\omega_n) \rangle_{S_0} \\ & \quad \langle \phi(\vec{q}, i\omega_n) \phi(-\vec{q}, -i\omega_n) \rangle_{S_0} = \end{aligned} \quad (\text{C25})$$

$$\begin{aligned} & \langle \phi(\vec{q}, i\omega_n) \phi(-\vec{q}, -i\omega_n) \rangle_{S_0} = \\ & Z_0^{-1} \prod_{\vec{q}, i\omega_n} \int d\text{Re} \phi(\vec{q}, i\omega_n) d\text{Im} \phi(\vec{q}, i\omega_n) \times \\ & \times \phi(\vec{q}, i\omega_n) \phi(-\vec{q}, -i\omega_n) e^{-\frac{1}{2} \hat{D}_0^{-1}(\vec{q}, i\omega_n) \phi(\vec{q}, i\omega_n) \phi(-\vec{q}, -i\omega_n)} \\ & = \frac{\partial \ln(Z_0)}{\partial \hat{D}_0^{-1}(\vec{q}, i\omega_n)} = \hat{D}_0(\vec{q}, i\omega_n) \end{aligned} \quad (\text{C26})$$

with $\hat{D}_0^{-1}(\vec{q}, i\omega_n) = (U/2)D_0^{-1}(\vec{q}, i\omega_n) = (U/2)[\delta + Aq'^2 + C|\omega_n|]$. Similarly, to Gaussian level

$$F_0 = -\frac{1}{\beta} \ln Z_0 = \frac{1}{2\beta} \sum_{\vec{q}, i\omega_n} \ln \hat{D}_0^{-1}(\vec{q}, i\omega_n), \quad (\text{C27})$$

up to a constant. Writing the quartic term as S_{int} , the full partition function is approximated by $Z \simeq Z_0[1 - \langle S_{int} \rangle_{Gauss} + \frac{1}{2} \langle S_{int}^2 \rangle_{Gauss}]$, with

$$\begin{aligned} \langle S_{int} \rangle_{Gauss} &= \tilde{u} \int_0^\beta d\tau \int d^2\vec{r} \langle \phi(\vec{r}, \tau)^4 \rangle_{Gauss} \\ &= 3\tilde{u} \int_0^\infty d\tau \int d^2\vec{r} [\langle \phi(\vec{r}, \tau)^2 \rangle]^2, \end{aligned} \quad (\text{C28})$$

and

$$\begin{aligned} \langle \phi(\vec{r}, \tau)^2 \rangle_{Gauss} &= \frac{1}{\beta V} \sum_{\vec{q}, i\omega_n} \langle \phi(\vec{q}, i\omega_n) \phi(-\vec{q}, -i\omega_n) \rangle_{S_0} \\ &= \frac{1}{\beta V} \sum_{\vec{q}, i\omega_n} \hat{D}_0(\vec{q}, i\omega_n). \end{aligned}$$

[The term in $\langle S_{int}^2 \rangle_{Gauss}$ will not be needed.]

The free energy Eq. C23 can thus be rewritten as

$$\begin{aligned} F &= \frac{1}{2\beta} \sum_{\vec{q}, i\omega_n} \ln D_0^{-1}(\vec{q}, i\omega_n) \\ &+ \frac{1}{2\beta} \sum_{\vec{q}, i\omega_n} (\delta_0 - \delta) D_0(\vec{q}, i\omega_n) \\ &+ \frac{3u}{\beta^2 N_0} [\sum_{\vec{q}, i\omega_n} D_0(\vec{q}, i\omega_n)]^2, \end{aligned} \quad (\text{C30})$$

with $u = \Pi_4/N_0\beta U^2$.

b. Stoner Factor

The variational parameter is found from $\partial F/\partial\delta = 0$, or

$$\delta = \delta_0 + \frac{12u}{\beta V} \sum_{\vec{q}, i\omega_n} D_0(\vec{q}, i\omega_n). \quad (\text{C31})$$

The next step is to carry out the sum over Matsubara frequencies and wave vectors. For the former, using

$$\begin{aligned} \frac{1}{\beta} \sum_{i\omega_n} X(i\omega_n) &= -\frac{1}{\beta\pi} \sum_{i\omega_n} \int_{-\infty}^\infty d\epsilon \frac{\text{Im}X(\epsilon + i\delta)}{i\omega_n - \epsilon} \\ &= -\int_0^\infty d\frac{\epsilon}{\pi} \coth \frac{\epsilon}{2T} \text{Im}X(\epsilon + i\delta), \end{aligned} \quad (\text{C32})$$

then

$$\begin{aligned} &\frac{1}{\beta V} \sum_{\vec{q}, i\omega_n} D_0(\vec{q}, i\omega_n) \\ &= \int \frac{d^2\vec{q}a^2}{(2\pi)^2} \int_0^{\alpha_\omega/C} \frac{d\epsilon}{\pi} \coth \frac{\epsilon}{2T} \frac{C\epsilon}{(\delta + Aq'^2)^2 + (C\epsilon)^2}. \end{aligned} \quad (\text{C33})$$

Note the sharp energy cutoff in Eq. C33. This comes about because the linear-in- ω dissipation is a result of Landau damping of the spin waves by electrons near the hot spots, and therefore the dissipation cuts off when the spin wave spectrum gets out of the electron-hole continuum. Numerical calculations (Fig. 11) show that the cutoff can be quite sharp, particularly near the VHS.

Equations C31, C33 can easily be solved in the limit $T = 0$. In this case, there is a transition at

$$\begin{aligned} \delta_0 &= -12u \int_0^{q_c^2} \frac{dq'^2 a^2}{4\pi} \int_0^{\alpha_\omega/C} \frac{d\epsilon}{\pi} \frac{C\epsilon}{(Aq'^2)^2 + (C\epsilon)^2} \\ &= -\frac{3uq_c^2 a^2}{\pi^2 C} R_0 \equiv 1 - \eta, \end{aligned} \quad (\text{C34})$$

$$R_0 = \frac{1}{2} \ln [1 + a_q^{-2}] + \frac{\tan^{-1}(a_q)}{a_q}, \quad (\text{C35})$$

(@20) $a_q = Aq_c^2/\alpha_\omega$. Since the right-hand side is finite and negative, fluctuations reduce but in general do not eliminate the order at $T = 0$. The quantum corrected Stoner criterion is $U\chi_0 = \eta$, where representative values of η are listed in Table I.

However, for finite T , there are corrections $\sim \ln(\delta)$, so δ cannot be set to zero, and there is no finite temperature transition (the Mermin-Wagner theorem is satisfied). To see this, it is adequate to approximate $\coth(x)$ as $1/x$ for $x \leq 1$ and 1 for $x > 1$. In this case, Eq. C31 can be solved exactly, Appendix A3. However, this exact solution is not very illuminating, and a simpler approximate solution will be given here. Since only the term proportional to T is singular, T and δ can be set to zero in the remaining term. Defining

$$\bar{\delta}_0 = \delta_0 + \eta - 1, \quad (\text{C36})$$

Eq. C31 becomes

$$\begin{aligned} \delta - \bar{\delta}_0 &= \frac{6uTa^2}{\pi^2 A} \int_\delta^{\delta + Aq_c^2} \frac{dy}{y} \tan^{-1} \left(\frac{2TC}{y} \right) \\ &\simeq \frac{3uTa^2}{\pi A} \ln \left(\frac{2CT}{\delta} \right), \end{aligned} \quad (\text{C37})$$

where the second line uses Eq. C50, below. Hence, there is no finite temperature phase transition, and δ only approaches zero asymptotically as $T \rightarrow 0$: approximately,

$$\delta = 2CTe^{-\pi A|\bar{\delta}_0|/3uTa^2}. \quad (\text{C38})$$

c. Susceptibility

The resulting susceptibility has NAFL form, Eq. 3, with (Eqs. C14,C18) the following explicit expressions:

$$\chi_{\vec{Q}} = \frac{\chi_0}{\delta} \quad (\text{C39})$$

$$\xi^2 = \frac{A}{\delta} \quad (C40)$$

$$\Delta^2 = \frac{\delta}{B} \quad (C41)$$

$$\omega_{sf} = \frac{\delta}{C} \quad (C42)$$

If the correlation length ξ is written in the form Eq. 16, and Eq. C51 is numerically solved for δ , then ρ_s is exactly given by

$$\rho_s = \frac{k_B T}{4\pi} \ln\left(\frac{A}{\xi_0^2 \delta}\right), \quad (C43)$$

with $\xi_0 = \sqrt{\frac{eA}{2TC}}$. Using Eq. C38, an approximate ρ_s is:

$$\rho_s^a = \frac{A|\bar{\delta}_0|}{12ua^2}. \quad (C44)$$

ρ_s is plotted in Fig. 15b, with $u^{-1} = 0.256\text{eV}$, chosen to give a ρ_s in agreement with the results of Chakravarty, et al.⁵⁸ for $x = 0$, $T = 0$.

3. ‘Exact’ Solution of Eq. C31

Approximating $\coth(x) = \max(1/x, 1)$, and introducing the notation $\bar{A}q_c^2 = Aq_c^2 + \delta$, $\bar{a}_q = \bar{A}q_c^2/\alpha_\omega$, and $t = 2TC$, the solution becomes

$$\delta - \delta_0 = \frac{3ua^2}{\pi^2 AC} [F_1 + F_2], \quad (C45)$$

with

$$\begin{aligned} F_1 &= \int_{\delta}^{\delta + Aq_c^2} dy \int_t^{\alpha_\omega} dx \frac{x}{x^2 + y^2} = \\ &\quad \frac{\bar{A}q_c^2}{2} \ln\left[\frac{1 + \bar{a}_q^2}{\bar{a}_q^2 + (t/\alpha_\omega)^2}\right] + \\ &\quad \alpha_\omega \tan^{-1}(\bar{a}_q) - \frac{\delta}{2} \ln\left[\frac{\delta^2 + \alpha_\omega^2}{\delta^2 + t^2}\right] - \alpha_\omega \tan^{-1}\left(\frac{\delta}{\alpha_\omega}\right) \end{aligned} \quad (C46)$$

$$\begin{aligned} F_2 &= t \int_{\delta}^{\delta + Aq_c^2} dy \int_0^t \frac{dx}{x^2 + y^2} = \\ &= t \int_{\delta}^{\delta + Aq_c^2} \frac{dy}{y} \tan^{-1}\left(\frac{t}{y}\right) = \\ &= t [I_1\left(\frac{t}{\bar{A}q_c^2}\right) - I_1\left(\frac{t}{\delta}\right)], \end{aligned} \quad (C47)$$

with

$$I_1(x) = I_0(\tan^{-1}(x)) - \tan^{-1}(x) \ln(x), \quad (C48)$$

$$I_0(x) = \int_0^x \ln(\tan \theta) d\theta = L(x) + L\left(\frac{\pi}{2} - x\right) - L\left(\frac{\pi}{2}\right), \quad (C49)$$

and $L(x) = -\int_0^x \ln(\cos t) dt$ is the Lobachevskiy function⁸⁶.

For most purposes, it can be assumed that $\delta \ll t \ll Aq_c^2, \alpha_\omega$, in which case $I_0(\tan^{-1}(x)) = \theta(\ln(\theta) - 1)$, with $\theta = \min\{x, 1/x\}$, and then F_2 , Eq. C47, simplifies.

$$\begin{aligned} F_2 &= \ln\left(\frac{t}{\delta}\right) [\delta + t \tan^{-1}\left(\frac{t}{\delta}\right)] + \delta - \frac{t^2}{Aq_c^2} \\ &\simeq \frac{\pi}{2} t \ln\left(\frac{t}{\delta}\right). \end{aligned} \quad (C50)$$

Defining $Z = 1 + (3ua^2/\pi^2 AC) \ln(\alpha_\omega/t)$, then

$$Z\delta - \bar{\delta}_0 = \frac{3ua^2 T}{\pi A} \ln\left(\frac{2CT}{\delta}\right), \quad (C51)$$

which agrees with Eq. C37 when $Z \rightarrow 1$.

APPENDIX D: PARAMETER EVALUATIONS

1. Hot Spots

Hot spots are defined as the intersection of the Fermi surface with the line $k_x + k_y = \pi/a$. At these points there is strong scattering, since the vector \vec{Q} connects two hot spots. The hot spots dominate the integrals A , B , Eqs. C19, C21 at $T = 0$. The Fermi functions limit the integral to a sum of approximately wedge-shaped areas centered on the hot spots, Fig. 12. In the main text, the susceptibilities were calculated numerically. Here, analytical approximations are introduced to clarify the role of the hot spots.

On a single wedge, a typical integral for, e.g., A becomes

$$\int \frac{d^2 \vec{q}}{(2\pi)^2} \frac{1}{(\epsilon_{\vec{k}+\vec{Q}} - \epsilon_{\vec{k}})^3} = \frac{1}{(4t)^3} \int \frac{d^2 \vec{q}}{(2\pi)^2} \frac{1}{(c_x + c_y)^3}. \quad (D1)$$

Letting $k_i = k_{i0} - k'_i$, $i = x, y$, then to lowest order the energy difference becomes

$$\begin{aligned} \Delta\epsilon &= \epsilon_{\vec{k}+\vec{Q}} - \epsilon_{\vec{k}} = \alpha_\theta k'(1 + \beta_\theta k') \\ &= \alpha_0 k_\perp (1 + \beta_0 k_\parallel), \end{aligned} \quad (D2)$$

with $\alpha_\theta = \alpha_0(\sin \theta + \cos \theta)$, $\beta_\theta = \beta_0(\sin \theta - \cos \theta)$, $\alpha_0 = 4ta s_{x0}$, and $\beta_0 = ac_{x0}/2s_{x0}$; k_\parallel and k_\perp are the momenta parallel and perpendicular to the zone diagonal (magnetic Brillouin zone boundary). The integral of Eq. D1 becomes

$$\frac{1}{4\pi^2} \int_{\theta_{min}}^{\theta_{max}} \frac{d\theta}{\alpha_\theta^3} \int \frac{dk'}{k'^2}, \quad (D3)$$

where θ_{min} and θ_{max} are the opening angles of the wedge. Thus, the integral over k' diverges at a hot spot. In this case, the expansion Eq. C18 must be modified.

2. A

The apparent singularity of A is an artifact. In reality, a finite q' shifts the location of the hot spots. To confirm this, the hot spot integrals can be evaluated as above. First, the shift in the positions of the hot spots is found, the points where $\epsilon_{\vec{k}-\vec{q}/2} = \epsilon_{\vec{k}+\vec{Q}+\vec{q}/2} = \mu$. Denoting the shift by (Eq. 6) $k_{x0}a \rightarrow k_{x0}a + \phi_x$, etc., then to first order in q , the shift is

$$\begin{aligned}\phi_x + \phi_y &= \frac{\tau c_{x0}}{2}(q_y - q_x), \\ \phi_y - \phi_x &= \frac{1}{2\tau c_{x0}}(q_y + q_x).\end{aligned}\quad (\text{D4})$$

Expanding about the shifted hot spots (with $k' =$ radial distance from new hot spots gives $\epsilon_{\vec{k}+\vec{Q}+\vec{q}/2} - \epsilon_{\vec{k}-\vec{q}/2} = 4tk'(\alpha_\theta(q) + \beta_\theta(q)k')$, where $\alpha_\theta(q) \rightarrow \alpha_\theta$ and $\beta_\theta(q) \rightarrow \beta_\theta$ as $q \rightarrow 0$. Hence, the integral to be evaluated is

$$\int_0^{k_c} dk' \left[\frac{1}{\alpha_\theta(q) + \beta_\theta(q)k'} - \frac{1}{\alpha_\theta + \beta_\theta k'} \right], \quad (\text{D5})$$

which is well behaved as a function of k' and can be expanded as a series in q^n . Note that there are terms linear in q , which are cancelled in averaging over the hot spots.

Since there are no singularities, direct numerical evaluation of $\chi(q') - \chi(q' = 0)$ is straightforward, yielding A , Fig. 13. [In the numerical calculation, some care is needed due to the terms linear in q . While they cancel when summed over all eight hot spots, to accurately determine the smaller quadratic term, this summation should be carried out at each k -point prior to summing the result for all k .]

3. A at the C-point

While the above analysis works for small q near the tip of the wedge, it is hard to extend it to the edge of the q -plateau, or in particular to the C-point, where the plateau width shrinks to zero. It is convenient to introduce a simplified model⁸⁷, for which the q -dependence of χ can be calculated *analytically*. It is convenient to recall Fig. 12. While the dashed lines in that figure represented an ω shift, they can equally well describe the q -shift of the energy denominator, Eq. D2. The plateau edge corresponds to the point where the dashed line intersects the Q-shifted FS (horizontal arrows). In the simplified model, the energy denominator is linearized, so $\Delta\epsilon \propto k_\perp$, independent of k_\parallel . Chosing \vec{q} to point along the (π, π) direction, the FS can be approximated by two circles of radius k_F , centered at (π, π) and $(-\pi, -\pi)$ (for the choice of \vec{q} the other two circles at $(\pi, -\pi)$ and $(-\pi, \pi)$ can be ignored). The Q-shifted FS is then a circle centered at $\Gamma = (0, 0)$. The FS at (π, π) and the Q-shifted FS are illustrated in Fig. 29c.

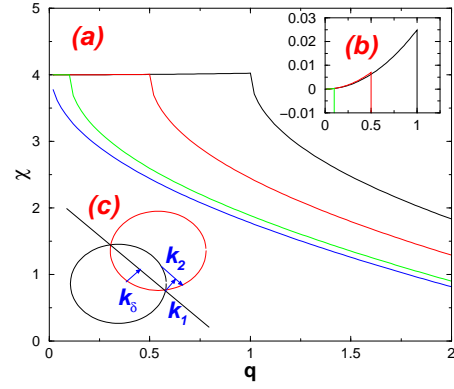


FIG. 29. (a) Calculated susceptibility $\chi(q)$ for several values of overlap δ . (b) Blowup of plateau region, for $\chi_q - \chi_{q=0}$. (c) Model of Fermi surfaces, defining δ , k_1 (k_\perp) and k_2 (k_\parallel).

Adding the contributions of the overlap of the Q-shifted FS with both the FS at (π, π) and the one at $(-\pi, -\pi)$, $\chi_q \propto I_{k_\delta+q} + I_{k_\delta-q}$, with

$$I = \int_0^{k_c} \frac{dk_\perp dk_\parallel}{k_\perp}, \quad (\text{D6})$$

where the region of integration is over the part of the upper FS in Fig. 29c not overlapped by the lower (Q-shifted) FS, and k_\perp ranges from zero at the apex of the wedge to the middle of the upper FS, $k_c = k_F - k_\delta$, where k_δ is the overlap parameter defined in Fig. 29c. To lowest order, for $k_\delta \ll k_F$,

$$\begin{aligned}I = 2\sqrt{2k_F k_\delta} &[\sqrt{1+\beta} + \ln \left| \frac{\sqrt{1+\beta} - 1}{\sqrt{1+\beta} + 1} \right| - \\ &- \Theta(1-\beta) (\sqrt{1-\beta} + \ln \left| \frac{\sqrt{1-\beta} - 1}{\sqrt{1-\beta} + 1} \right|)],\end{aligned}\quad (\text{D7})$$

with $\beta = k_c/k_\delta$ and Θ the unit step function. The expression for $I_{k_\delta-q}$ must be modified when $q > k_\delta$ and the two FSs no longer overlap⁸⁷: $I_{k_\delta-q} = 2\sqrt{2k_F} [1 - \gamma \tan^{-1} 1/\gamma]$, with $\gamma = \sqrt{(q - k_\delta)/2k_F}$. The calculated susceptibilities, Fig. 29a, display the flat topped plateaus with weak positive curvature ($A < 0$, Fig. 29b). At the plateau edge the susceptibility falls sharply, $\chi \sim 1 - \pi\gamma/2 \sim \sqrt{q}$. The C-point corresponds to $k_\delta = 0$.

4. B

The expression for B may be written exactly as the $\omega \rightarrow 0$ limit of

$$B = U \text{Re} \sum_{\vec{k}} \left[\frac{f(\epsilon_{\vec{k}}) - f(\epsilon_{\vec{k}+\vec{Q}})}{(\epsilon_{\vec{k}+\vec{Q}} - \epsilon_{\vec{k}})} \right] \frac{1}{((\epsilon_{\vec{k}+\vec{Q}} - \epsilon_{\vec{k}})^2 - \omega^2)} \quad (\text{D8})$$

It can be shown that B has a logarithmic correction due to the hot spots. The integral can be approximately evaluated by (a) using symmetry to reduce the integral to one over an octant of the Brillouin zone containing one hot spot, (b) splitting the domain of integration into (i) a circle of radius k_c about the hot spot, and (ii) the remainder of the domain, and (c) numerically evaluating the integral over domain (ii) while providing an analytic approximation to that over (i). Then the k integral over the hot spot circle can be written approximately as

$$I = \int_0^{k_c} \frac{(1 - 3\beta_\theta k) dk}{\alpha_\theta^2 k^2 - \omega^2} \simeq \frac{1}{\alpha_\theta^2} \left[\frac{1}{k_c} - 3\beta_\theta \log \frac{\alpha_\theta k_c}{\omega} \right]. \quad (\text{D9})$$

At $T = 0$, the integral I must then be integrated in θ over the wedge where the difference in Fermi functions does not vanish. The integral from outside the hot spot circle will eliminate the k_c -dependence, but should not affect the $\log(\omega)$ term. The same logarithmic divergence can be found as a byproduct of the calculation of C , below.

It is difficult to directly evaluate the two-dimensional principal value integral for B . Instead, it is much simpler to evaluate $\text{Re}(\chi)$ via Kramers-Kronig transformation of $\text{Im}(\chi)$ and find B by numerical differentiation. When this is done, it is found that (a) B is numerically very small due to the plateau in $\text{Re}(\chi)$, Fig. 10d, and (b) the logarithmic correction is too small to determine accurately.

5. C

Parameter C is conveniently found by analytically continuing Eq. D8 back to the Matsubara frequencies,

$$\frac{C}{|\omega_n|} = U \sum_{\vec{k}} \left[\frac{f(\epsilon_{\vec{k}}) - f(\epsilon_{\vec{k}+\vec{Q}})}{(\epsilon_{\vec{k}+\vec{Q}} - \epsilon_{\vec{k}})} \right] \frac{1}{((\epsilon_{\vec{k}+\vec{Q}} - \epsilon_{\vec{k}})^2 + \omega_n^2)}. \quad (\text{D10})$$

The wedge integral can be evaluated as for B . The relevant integral is

$$I \simeq \int_0^{k_c} \frac{dk(1 - 3\beta_\theta k)}{k^2 + \hat{\omega}_n^2} \simeq \frac{1}{\hat{\omega}_n} \tan^{-1} \left(\frac{k_c}{\hat{\omega}_n} \right) - \frac{3\beta_\theta}{2} \ln \left(1 + \left(\frac{k_c}{\hat{\omega}_n} \right)^2 \right) \simeq \frac{\pi}{2\hat{\omega}_n} - \frac{1}{k_c} - 3\beta_\theta \ln \left(\frac{k_c}{\hat{\omega}_n} \right), \quad (\text{D11})$$

($\hat{\omega}_n = \omega_n/\alpha_\theta$) thus giving both the linear in ω dissipation, and confirming the $\ln(\omega)$ divergence found above. Figure 11 shows the divergence of C as μ approaches the VHS. Note that it is cut off at increasingly lower frequencies: the arrows correspond to $\omega_n = \pi C$.

Alternatively, Eq. C22 may be used; this can be integrated to yield Eq. 14 (in agreement with Sachdev, et al.⁵⁷), explicitly displaying the divergence at the VHS ($s_{x0} \rightarrow 0$).

6. u

Since there is some controversy^{34,31} concerning u , it shall be evaluated in detail. Millis³⁴ showed that for free electrons (parabolic bands) this expression is in general well defined, but diverges when \vec{Q} is a ‘spanning’ vector of the Fermi surface – in the present case, this would correspond to the H- and C-points. Abanov, et al.³¹ found a more severe divergence: u diverges for all μ in the hot spot regime. The problem lies in the limit of external frequencies $\rightarrow 0$, momenta $\rightarrow 0$ or \vec{Q} . Taking this limit on the momenta, the expression for u can be written as

$$u = \frac{U^2}{N_0 \beta} \sum_{\vec{k}, i\omega_n} \frac{1}{(\epsilon_{\vec{k}} - i\omega_n)(\epsilon_{\vec{k}} - i\omega_n + i\omega_4)} \times \frac{1}{(\epsilon_{\vec{k}+\vec{Q}} - i\omega_n - i\omega_1)(\epsilon_{\vec{k}+\vec{Q}} - i\omega_n - i\omega_1 - i\omega_2)}. \quad (\text{D12})$$

The sum over Matsubara frequencies yields

$$u = U^2 \sum_{\vec{k}} \left[\frac{f(\epsilon_{\vec{k}})}{i\omega_4} \left(\frac{1}{(i\omega_3 - \Delta\epsilon)(i\omega_3 + i\omega_2 - \Delta\epsilon)} - \frac{1}{(i\omega_1 + \Delta\epsilon)(i\omega_1 + i\omega_2 + \Delta\epsilon)} \right) + \frac{f(\epsilon_{\vec{k}+\vec{Q}})}{i\omega_2} \left(\frac{1}{(i\omega_3 - \Delta\epsilon)(i\omega_1 + i\omega_2 + \Delta\epsilon)} - \frac{1}{(i\omega_1 + \Delta\epsilon)(i\omega_3 + i\omega_2 - \Delta\epsilon)} \right) \right], \quad (\text{D13})$$

where $\Delta\epsilon = \epsilon_{\vec{k}} - \epsilon_{\vec{k}+\vec{Q}}$. Letting $\omega_{i,\pm} = (\omega_i \pm \omega_{i+2})/2$ ($i = 1, 2$), and noting that $\omega_{1+} = -\omega_{2+}$, this simplifies to

$$u = 2U^2 \sum_{\vec{k}} \frac{(f(\epsilon_{\vec{k}+\vec{Q}}) - f(\epsilon_{\vec{k}}))W_-}{(W_-^2 + \omega_{1+}^2)(W_-^2 + \omega_{2-}^2)}, \quad (\text{D14})$$

where

$$W_- = (i\omega_{1-} + \Delta\epsilon). \quad (\text{D15})$$

Thus in Matsubara frequency space, u is largest for $\omega_{1+} = \omega_{2-} = 0$, so it should indeed be reasonable to estimate it in that limit:

$$u(i\omega_1, 0, 0) = U^2 \frac{\partial^2}{\partial(i\omega_1)^2} \sum_{\vec{k}} \frac{f(\epsilon_{\vec{k}+\vec{Q}}) - f(\epsilon_{\vec{k}})}{i\omega_1 + \Delta\epsilon}. \quad (\text{D16})$$

In turn, it should be possible to approximate u , Eq. D16, by its $\omega_1 \rightarrow 0$ limit, if this is nonsingular. From Eq. C18,

$U\chi_0(\vec{Q}, \omega) = B\omega^2 + iC\omega + 1 - \delta_0$. Thus, the analytic continuation $i\omega_1 \rightarrow \omega + i\delta$ yields

$$u(0, 0, 0) = U^2 \lim_{\omega \rightarrow 0} \frac{\partial^2 \chi_0(\vec{Q}, \omega)}{\partial \omega^2} \simeq 2BU. \quad (\text{D17})$$

Due to the plateau in $\chi(\vec{Q}, \omega)$, B (Table I) and hence u are extremely small. The smallness of u is true only in the limit that all external frequencies are small, which means that a more complicated expression should be used to evaluate u . Moreover, there is an additional problem: as found above, B has a correction in $\ln(\omega)$, which would formally be divergent. Hence, the model is not fully self-consistent, and u will be treated as an empirical parameter. The weak logarithmic divergence will be neglected, and u approximated by a constant.

APPENDIX E: INTERLAYER COUPLING

1. Dispersion of t_z : Direct and Staggered Stacking

Andersen, et al.⁸⁸ demonstrated that the anomalous form of interlayer hopping in the cuprates, $t_z = t_{z0}(c_x - c_y)^2$, could be understood by coupling the $\text{Cu}_{d_x^2-d_y^2}$ and O_p orbitals to the Cu_{4s} orbitals, which have significant interlayer coupling. Here, I provide a simplified calculation including only these orbitals, and show how the dispersion is modified by staggered stacking of the CuO_2 layers. For uniform stacking (Cu above Cu), the hopping matrix becomes

$$H = \begin{pmatrix} \Delta & -2ts_x & 2ts_y & 0 \\ -2ts_x & 0 & 0 & -2t_{ps}s_x \\ 2ts_y & 0 & 0 & -2t_{ps}s_y \\ 0 & -2t_{ps}s_x & -2t_{ps}s_y & \Delta_s + E_{sz} \end{pmatrix}, \quad (\text{E1})$$

with $s_i = \sin k_i a/2$. Here the first (last) row is for the $\text{Cu}_{d_x^2-d_y^2}$ (Cu_{4s}) orbital, and the middle rows are for the O_{px} and O_{py} orbitals, with $E_{sz} = -4t_{sz} \cos k_z c$. In the limit $\Delta_s + E_{sz} \gg \Delta \gg t, t_{ps}$, the antibonding band has dispersion

$$E = \Delta - \frac{2t^2}{\Delta}(c_x + c_y - 2) - \frac{4t^2 t_{ps}^2}{\Delta^2(\Delta_s + E_{sz})}(c_x - c_y)^2, \quad (\text{E2})$$

so if $t_{sz} \ll \Delta_s$, the interlayer hopping has the form $t_{z0} \cos k_z c (c_x - c_y)^2$, with $t_{z0} = -16t^2 t_{ps}^2 t_{sz} / \Delta^2 \Delta_s^2$. While this form had been suggested earlier⁸⁹ and found experimentally for the bilayer splitting in BSCCO⁹⁰, it should be noted that it is only approximate, and that, at least in YBCO, there is considerable splitting of the bilayer bands along the zone diagonal⁸⁸. Nevertheless, this form is adequate for the present purposes.

When successive layers are staggered, the only modification to the hopping matrix is in the form of $E_s(k_z)$, which now acquires an in-plane dispersion,

$$\begin{aligned} E_s(k_z) &= -4t_{sz} \cos k_z c [\cos(k_x + k_y)a/2 + \cos(k_x - k_y)a/2] \\ &= -8t_{sz} \cos k_z c \cos k_x a/2 \cos k_y a/2, \end{aligned} \quad (\text{E3})$$

which leads to Eq. 24.

2. Estimation of t_z from Resistivity Anisotropy

The dc conductivity can be estimated

$$\sigma_{ii} = \frac{2e^2}{\Omega} \sum_{\vec{k}} v_i^2 \delta(\epsilon_{\vec{k}} - \mu) \tau_{\vec{k}}, \quad (\text{E4})$$

$i = x, y, z$, with Ω the unit cell volume, $v_i = \hbar^{-1} d\epsilon_{\vec{k}}/dk_i$, and $\tau_{\vec{k}}$ the scattering rate. Recent ARPES data suggest that, when bilayer splitting is resolved, $\tau_{\vec{k}}$ is relatively isotropic over the Fermi surface⁹¹. Taking $\tau_{\vec{k}}$ independent of \vec{k} , the conductivities are given by integrals over the Fermi surface. Figure 30a shows a normalized conductivity ratio,

$$\frac{\hat{\sigma}_{zz}}{\sigma_{xx}} = \frac{at^2}{ct_{z0}^2} \frac{\sigma_{zz}}{\sigma_{xx}}, \quad (\text{E5})$$

while Fig. 30b shows the resulting normalized interlayer hopping $\hat{t}_{z0} = t_{z0} \sqrt{c/a}$, which would be required to produce a resistivity anisotropy $\rho_{zz}/\rho_{xx} = 1000$. For simplicity, it is assumed that t_{z0} is small, and $\hat{\sigma}_{zz}/\sigma_{xx}$ is evaluated in the limit $t_{z0} \rightarrow 0$. It can be seen that (a) the staggered stacking reduces the conductivity by approximately a factor of 20, independent of doping (except near the VHS), so (b) assuming the resistivity anisotropy is 1000 for optimally doped LSCO, it is estimated that $t_{z0}/t = 0.11$ (for staggered stacking) or 0.025 (for uniform stacking).

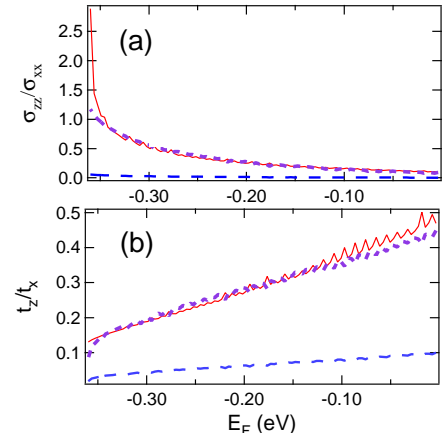


FIG. 30. (a) Normalized conductivity ratio, $\hat{\sigma}_{zz}/\sigma_{xx}$ vs doping E_F , for uniform (solid line) and staggered stacking (long dashed line and short dashed line, $\times 20$); and (b) resulting normalized interlayer hopping \hat{t}_{z0} for staggered (solid line) and uniform stacking (long dashed line and short dashed line, $\times 4.5$).

3. z-Component of Ordering Vector

Given a finite interlayer hopping t_z , the first issue is to identify the three-dimensional ordering vector: what Q_z minimizes the free energy? At mean field level, the initial magnetic instability will be associated with the state for which the RPA denominator first diverges, i.e., the state with the largest value of $Re\chi_0(\vec{Q}, Q_z)$. (Note that these calculations implicitly assume that the two-dimensional ground state involves commensurate order at \vec{Q} .) For uniform stacking, a complicated dependence on doping, temperature, and t_z is found. Figures 31,32 plot χ_0 vs chemical potential for $T = 100K, 10K$, respectively. The shift of the susceptibility peak with doping can readily be understood by comparison with Fig. 1. Both temperature and interlayer coupling act to smear out the VHS, and in both cases cause the susceptibility peak to shift to smaller chemical potential (lower hole doping), Fig. 31d. Note that the peak shifts at different rates for different Q_z -values, showing that the band is developing a considerable c-axis dispersion. The fastest shift (short dashed line in Fig. 31d, corresponding to $Q_z = 0$) can thus be considered as representing a crossover from quasi-two-dimensional to fully three dimensional dispersion.

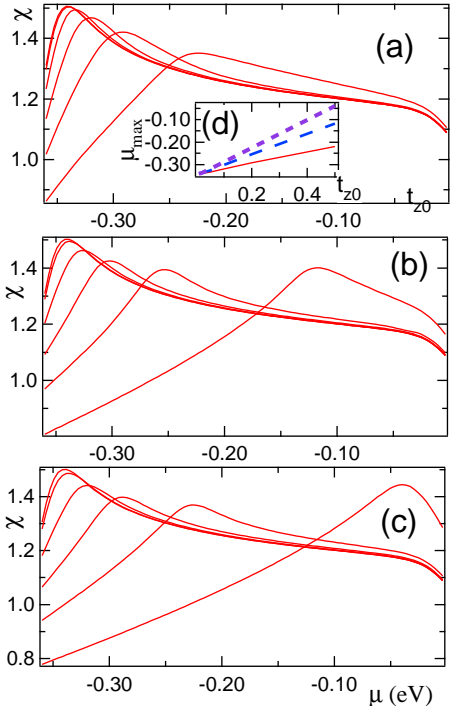


FIG. 31. $\chi_0(\vec{Q}, Q_z)$ at $T = 100K$ vs chemical potential μ , for uniform stacking and $Q_z = \pi$ (a), $\pi/2$ (b), and 0 (c). The various curves correspond to $t_{z0}/t = 0.01, 0.02, 0.05, 0.1, 0.2$, and 0.5, with the peak in χ_0 shifting to the right with increasing t_{z0} . Inset (d): position of peak, μ_{max} , vs t_{z0} for $Q_z = \pi$ (solid line), $\pi/2$ (long dashed line), and 0 (short dashed line).

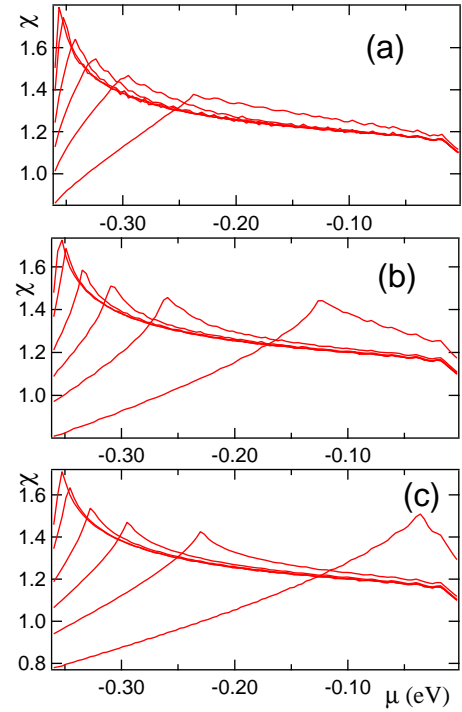


FIG. 32. $\chi_0(\vec{Q}, Q_z)$ vs chemical potential μ , as in Fig. 31, but at $T = 10K$.

This dispersive shift of the peak in χ_0 leads to a doping dependence of the optimal Q_z , as illustrated in Fig. 33 for $t_{z0} = 0.2t$. For large hole doping, near the $t_{z0} = 0$ VHS, the susceptibility maximum corresponds to $Q_z = \pi/c$, while near the susceptibility peak, the spin modulation becomes incommensurate (intermediate values of Q_z have the largest susceptibility). There is a rapid evolution of the optimal Q_z , and beyond the peak regime, over essentially the entire electron-doped regime, the optimal Q_z is 0. This same pattern is repeated for smaller t_{z0} , with only the region of the susceptibility peak changing. The results are essentially independent of the sign of t_z .

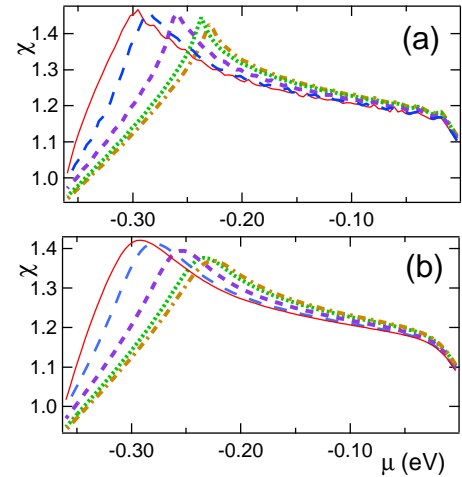


FIG. 33. $\chi_0(\vec{Q}, Q_z)$ vs chemical potential μ , for uniform stacking and $t_{z0} = 0.2t$, and $T = 10K$ (a), or $100K$ (b), with $Q_z/\pi = 1$ (solid line), 0.75 (long dashed line), 0.5 (short dashed line), 0.25 (dotted line), 0 (dot-dashed line).

4. Calculation of A_z

a. Uniform Stacking

Given t_z and Q_z , the parameter A_z of Eq. 2 can be evaluated: $U\chi(\vec{Q} + q_z\hat{z}, \omega = 0) = U\chi(\vec{Q} + Q_z\hat{z}, 0) + A_z(q_z - Q_z)^2$. The dominant ordering vectors, $Q_z = \pi/c$ and $Q_z = 0$, can be analyzed in more detail. For the former choice,

$$A_z^\pi = \frac{Uc^2}{4} \sum_{\vec{k}} \left[\frac{t_z c_z}{\epsilon_{\vec{k}} - \epsilon_{\vec{k}+\vec{Q}} + i\delta} \left(2 \frac{f_{\vec{k}} - f_{\vec{k}+\vec{Q}}}{\epsilon_{\vec{k}} - \epsilon_{\vec{k}+\vec{Q}} + i\delta} - [f'_{\vec{k}} + f'_{\vec{k}+\vec{Q}}] \right) - 2t_z^2 s_z^2 \left(\frac{f''_{\vec{k}} - f''_{\vec{k}+\vec{Q}}}{\epsilon_{\vec{k}} - \epsilon_{\vec{k}+\vec{Q}} + i\delta} \right) \right], \quad (E6)$$

with $f'_{\vec{k}} = -f_{\vec{k}}(1 - f_{\vec{k}})/k_B T$, $f''_{\vec{k}} = -f'_{\vec{k}}(1 - 2f_{\vec{k}})/k_B T$, $c_z = \cos k_z c$, $s_z = \sin k_z c$. For the latter case

$$A_z^0 = \frac{-Uc^2}{4} \sum_{\vec{k}} \left[t_z c_z \left(\frac{f'_{\vec{k}} - f'_{\vec{k}+\vec{Q}}}{\epsilon_{\vec{k}} - \epsilon_{\vec{k}+\vec{Q}} + i\delta} \right) + 2t_z^2 s_z^2 \left(\frac{f''_{\vec{k}} - f''_{\vec{k}+\vec{Q}}}{\epsilon_{\vec{k}} - \epsilon_{\vec{k}+\vec{Q}} + i\delta} \right) + 8 \frac{f_{\vec{k}} - f_{\vec{k}+\vec{Q}}}{(\epsilon_{\vec{k}} - \epsilon_{\vec{k}+\vec{Q}} + i\delta)^3} - 4 \frac{f'_{\vec{k}} + f'_{\vec{k}+\vec{Q}}}{(\epsilon_{\vec{k}} - \epsilon_{\vec{k}+\vec{Q}} + i\delta)^2} \right]. \quad (E7)$$

Figure 34 (35a) shows how $\chi_0(\vec{Q}, Q_z)$ varies with Q_z for $t_{z0} = 0.1t$ (0.02t), for a number of different dopings. For the entire electron-doped regime, the peak is at $Q_{zm} = 0$ (Fig. 34b, 35d), crossing over to $Q_{zm} = \pi/c$ in the hole doped regime. Away from the peak, the susceptibility varies as $\hat{A}_z q_z^2$, with $q_z = Q_z - Q_{zm}$, and in the electron-doped regime the full variation can be approximated by a cosine. The amplitude of the cosine falls to zero as the C-point is approached. In the quasi-two-dimensional regime this amplitude scales with t_{z0}^2 . Figure 35b,c shows plots of the best parabolic fit to $A'_z = \hat{A}_z/c^2$ for $t_{z0}/t = 0.02$ (squares) and 0.1 (triangles). For $t_{z0}/t = 0.1$, an alternative A'_z is shown, found by fitting the full susceptibility as a cosine in q_z (circles). The good agreement between the two techniques shows that this is a reasonable approximation in the electron-doped regime ($-0.2eV \leq \mu \leq 0$). Near the susceptibility peak, the variation is nonsinusoidal, and the parabolic fit leads to a large value for A'_z .

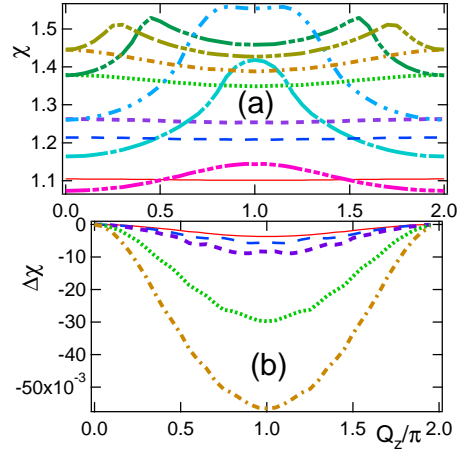


FIG. 34. (a) $\chi_0(\vec{Q}, Q_z)$ vs Q_z for $t_{z0} = 0.1t$, and $T = 10K$, and a variety of chemical potentials $\mu = -0.003559$ (solid line), -0.08898 (long dashed line), -0.1779 (short dashed line), -0.2669 (dotted line), -0.2847 (dot-dashed line), -0.2954 (long-long-short-short dashed line), -0.3025 (long-short-short dashed line), -0.3203 (dash-dot-dot line), -0.3381 (long-short dashed line), and -0.3559 meV (long-short-short-short dashed line). (b) $\Delta\chi = \chi_0(\vec{Q}, Q_z) - \chi_0(\vec{Q}, Q_z = 0)$, where the curves have the same meaning as in frame (a).

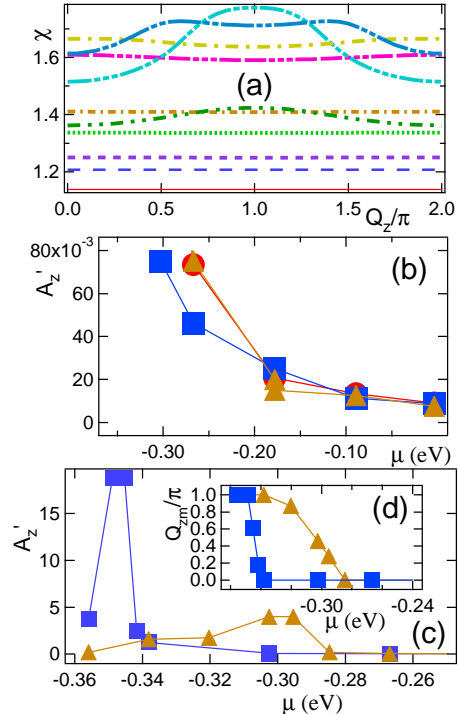


FIG. 35. (a) $\chi_0(\vec{Q}, Q_z)$ vs Q_z for $t_{z0} = 0.02t$, and $T = 10K$, and a variety of chemical potentials $\mu = -0.003559$ (solid line), -0.08898 (long dashed line), -0.1779 (short dashed line), -0.2669 (dotted line), -0.3025 (dot-dashed line), -0.3381 (long-long-short-short-short dashed line), -0.3417 (long-dashed-dotted line), -0.3452 (long-short-short dashed line), -0.3488 (long-short-short-short dashed line), and -0.3559 meV (long-dash-dot-dotted line). (b,c) $A'_z = A_z/Uc^2$ vs μ for $t_{z0}/t = 0.02$ (squares, $A'_z \times 25$) and 0.1 (triangles, circles). (d) Q_{zm} vs μ for $t_{z0}/t = 0.02$ (squares) and 0.1 (triangles).

b. Staggered Stacking

The same calculations can be repeated for the t_z of Eq. 24, associated with staggered stacking; Fig. 36a shows A_z calculated from Eqs. E6, E7 at $Q_z = 0$ (solid lines) and π (dashed lines). The frustration induced by staggering of the CuO₂ layers is reflected in a strong suppression of the q_z -dependence of χ , which leaves a small residual contribution quadratic in t_{z0} , Fig. 36b. Since t_z vanishes at $(\pi, 0)$, there is no shift of the susceptibility peak with doping. Note the symmetry of the A_z values between 0 and π . In fact, $\chi(Q_z)$ is closely sinusoidal, particularly for small t_{z0} , with maxima either at π or 0. Thus, near either the H- or C-points, the maximum of χ corresponds to $Q_z = \pi$. For intermediate dopings, $Q_z = 0$ is favored. At two distinct chemical potentials, the amplitude of the cosine collapses and changes sign. At the crossing points, χ is independent of Q_z , leading formally to $T_N \rightarrow 0$. Note from Fig. 36c that the suppression of A_z is approximately in the same ratio as that of the resistivity, found above.

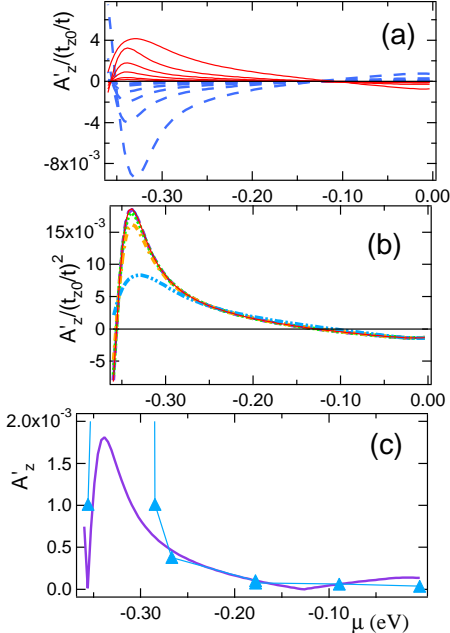


FIG. 36. (a) $A'_z = A_z/Uc^2$ vs chemical potential μ for $Q_z = 0$ (solid lines) or π (dashed lines), for a variety of values of t_{z0} and $T = 100K$. In order of increasing amplitude, the values are $t_{z0}/t = 0.01, 0.02, 0.05, 0.1, 0.2, \text{ and } 0.5$. (b) Scaling of $A'_z(0)$ with $(t_{z0}/t)^2$. Curves are $t_{z0}/t = 0.01$ (solid line), 0.02 (long dashed line), 0.05 (short dashed line), 0.1 (dotted line), 0.2 (dot-dashed line), and 0.5 (dot-dot-dashed line). (c) Comparison of $\max(A_z)$ for staggered stacking (solid line) and uniform stacking (triangles, $\times 1/20$) at $t_{z0}/t = 0.1$.

5. Calculation of T_N

When there is a finite interlayer hopping t_z , Eq.C37 becomes

$$\delta - \bar{\delta}_0 = \frac{6uTa^2c}{\pi^2 A} \int_0^{\frac{\pi}{c}} \frac{dq_z}{\pi} \int_{y_0}^{y_0 + Aq_z^2} \frac{dy}{y} \tan^{-1}\left(\frac{2TC}{y}\right) \simeq \frac{3uTa^2}{\pi A} \ln\left(\frac{T}{T_{3D}}\right), \quad (E8)$$

where $y_0 = \delta + A_z q_z^2$ and $T_{3D} = \pi^2 A_z / 2Ce^2c^2$. (A small correction to $\bar{\delta}_0$ is neglected. Treating the q_z dependence as a cosine rather than a cutoff quadratic leads to qualitatively similar results.) Thus a finite A_z always cuts off the divergence found in Eq.C37, leading to a finite T_N whenever there is a zero-temperature Neel state (e.g., up to a QCP). It should be noted that the above calculation implicitly assumed that $T > T_{3D} \sim A_z$: for $T < T_{3D}$ the logarithm is cut off and the system behaves like an anisotropic three-dimensional magnet. For $t_{z0}/t < 0.1$, the system is generally in the quasi-two-dimensional limit, Fig. 37a. Figure 37b compares the mean-field Neel transition with the Neel transition found assuming uniform stacking and finite interlayer couplings $t_{z0}/t = 0.1, 0.02$, and 2×10^{-6} [the last found by scaling the T_{3D} for $t_{z0}/t = 0.02$ by the ratio of t_{z0}^2 's]. It is seen that $T_N \rightarrow 0$ as $t_{z0} \rightarrow 0$, albeit exceedingly slowly.

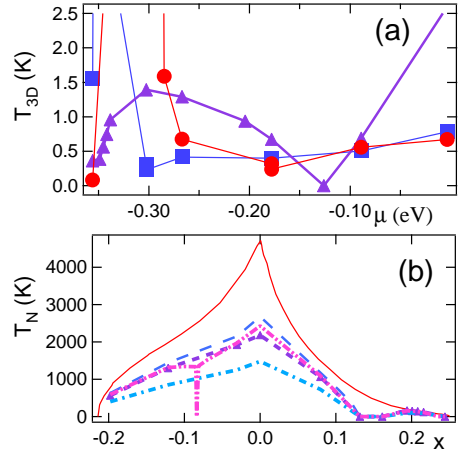


FIG. 37. (a) T_{3D} vs μ for $T = 10K$ and uniform stacking with $t_{z0} = 0.1t$ (circles, $\times 1/25$) or 0.02 (squares), or staggered stacking with $t_{z0}=0.02$ (triangles). (b) T_N vs x , comparing mean field transition (solid line) with interlayer coupling models (uniform stacking) assuming $t_{z0}/t = 0.1$ (long dashed line), 0.02 (short dashed line), and 2×10^{-6} (dot-dashed line), and the staggered stacking model assuming $t_{z0}/t = 0.1$ (dot-dot-dash line).

The above calculations are for uniform stacking. For staggered stacking A_z is reduced, in approximately the same ratio as the resistivities. Hence, the staggered stacking with $t_{z0}/t = 0.1$ should be comparable to uniform stacking with $t_{z0}/t = 0.02$, as observed, Fig. 37. While T_N technically goes to zero for staggered stacking near $x = -0.0838$, the decrease is logarithmic, and in practice no more than a weak dip is expected to be observed (the point with $T_N = 0K$ is omitted from the plot in Fig. 25). Hence, if t_{z0} is estimated from the resistivity, it will be nearly impossible to distinguish uniform from staggered stacking via measurements of T_N .

In the above calculations, a constant value of A was assumed for each doping, as given in Fig. 13. In fact, for the electron-doped cuprates, $A \sim 1/T^{1.5}$ for $T > T_A^*$, Fig. 9. This would cause an enhancement of the logarithmic correction, $\sim T^{2.5}$, tending to pin T_N close to T_A^* . For the present parameter values, this could reduce T_N by roughly a factor of two, still larger than the experimental values.

A more likely source of the discrepancy is the possible temperature dependence of U_{eff} , Appendix B. The large U_{eff} at half filling arises from lack of screening, in the presence of a Mott gap – and is appropriate in analyzing the low- T Fermi surfaces found in ARPES. For calculating the onset of the Mott gap, the mean field T_N , it is more appropriate to use the paramagnetic susceptibility, as in Fig 28a. When this is done, considerably smaller transition temperatures are found, both at the mean field level, Fig. 38a, and when fluctuations and interlayer hopping are included, Fig. 38b. While the latter are closer to the experimental values, no attempt has been made to correct U_{eff} for the short range gap.

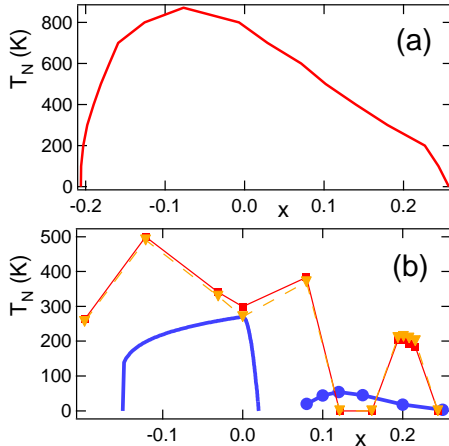


FIG. 38. (a) Mean field T_N vs x assuming paramagnetic U_{eff} (Appendix B). (b) Corresponding T_N vs x , calculated using Eq. E8. Squares = staggered stacking with $t_{z0}/t = 0.1$; triangles = uniform stacking with $t_{z0}/t = 0.02$; solid line and circles = data, as in Fig. 25.

- ¹ J.R. Schrieffer, X.G. Wen, and S.C. Zhang, Phys. Rev. B**39**, 11663 (1989).
- ² A. Kampf and R.W. Schrieffer, Phys. Rev. B**42**, 7967 (1990).
- ³ Y.M. Vilk and A.-M.S. Tremblay, J. Phys. I **7**, 1309 (1997); B. Kyung, J.S. Landry, D. Poulin, and A.-M.S. Tremblay, cond-mat/0112273.
- ⁴ N.E. Bickers, D.J. Scalapino, and S.R. White, Phys. Rev. Lett. **62**, 961 (1989).
- ⁵ H. Schulz, J. Phys. (Paris) **50**, 2833 (1989); D. Poilblanc and T.M. Rice, Phys. Rev. B**39**, 9749 (1989); J. Zaanen and O. Gunnarsson, *ibid.* B**40**, 7391 (1989); B.I. Shraiman and E.D. Siggia, Phys. Rev. Lett. **62**, 1564 (1989).
- ⁶ H.J. Schulz, Phys. Rev. Lett. **65**, 2462 (1990); C. Zhou and H.J. Schulz, Phys. Rev. B**52**, 11557 (1995).
- ⁷ J.M. Tranquada, B.J. Sternlieb, J.D. Axe, Y. Nakamura, and S. Uchida, Nature **375**, 561 (1995); J.M. Tranquada, J.D. Axe, N. Ichikawa, A.R. Moodenbaugh, Y. Nakamura, and S. Uchida, Phys. Rev. Lett. **78**, 338 (1997).
- ⁸ K.M. Lang, V. Madhavan, J.E. Hoffman, E.W. Hudson, H. Eisaki, S. Uchida, and J.C. Davis, Nature **415**, 412 (2002).
- ⁹ M. Matsuda, M. Fujita, K. Yamada, R.J. Birgeneau, Y. Endoh, and G. Shirane, cond-mat/0111228.
- ¹⁰ N.P. Armitage, D.H. Lu, C. Kim, A. Damascelli, K.M. Shen, F. Ronning, D.L. Feng, H. Eisaki, Z.-X. Shen, P.K. Mang, N. Kaneko, M. Greven, Y. Onose, Y. Taguchi, and Y. Tokura, Phys. Rev. Lett. **88**, 257001 (2002).
- ¹¹ C. Kusko, R.S. Markiewicz, M. Lindroos, and A. Bansil, Phys. Rev. B**66**, 140513 (2002).
- ¹² R.S. Markiewicz and C. Kusko, Phys. Rev. B**65**, 064520 (2002).
- ¹³ C. Kusko and R.S. Markiewicz, unpublished.
- ¹⁴ R. Zitzler, Th. Pruschke, and R. Bulla, to be published, Euro. Phys. Jnl., cond-mat/0201145.
- ¹⁵ A. Singh and Z. Tešanović, Phys. Rev. B**41**, 614 (1990).
- ¹⁶ A.V. Chubukov and D.M. Frenkel, Phys. Rev. B**46**, 11884 (1992).
- ¹⁷ M. Suzuki, S. Kubo, K. Ishiguro, and K. Haruna, Phys. Rev. B**50**, 9434 (1994); W. Jiang, S.N. Mao, X.X. Xi, X. Jiang, J.-L. Peng, T. Venkatesan, C.J. Lobb, and R.L. Greene, Phys. Rev. Lett. **73**, 1291 (1994).
- ¹⁸ C. Sire, C.M. Varma, A.E. Ruckenstein, and T. Giamarchi, Phys. Rev. Lett. **72**, 2478 (1994).
- ¹⁹ C. Castellani, C. Di Castro, and M. Grilli, Phys. Rev. Lett. **75**, 4650 (1995).
- ²⁰ R.S. Markiewicz, unpublished.
- ²¹ J.L. Tallon, J.W. Loram, G.V.M. Williams, J.R. Cooper, I.R. Fisher, J.D. Johnson, M.P. Staines, and C. Bernhard,

Phys. Stat. Sol. b**215**, 531 (1999).

²² R.S. Markiewicz, Physica C**169**, 63 (1990).

²³ S. Andergassen, S. Caprara, C. Di Castro, M. Grilli, Phys. Rev. Lett. **87**, 056401 (2001).

²⁴ K. K. Murata and S. Doniach, Phys. Rev. Lett. **29**, 285 (1972).

²⁵ T. Moriya, "Spin Fluctuations in Electron Magnetism", (Springer, Berlin, 1985).

²⁶ H. Hasegawa and T. Moriya, J. Phys. Soc. Jpn. **36**, 1542 (1974).

²⁷ P.A. Lee, T.M. Rice, and P.W. Anderson, Sol. St. Commun. **14**, 703 (1974).

²⁸ W. Götze L. and Sjögren, Rep. Prog. Phys. **55**, 241 (1992).

²⁹ T. Moriya, Y. Takahashi, and K. Ueda, J. Phys. Soc. Jpn., **59**, 2905 (1990).

³⁰ P. Monthoux and D. Pines, Phys. Rev. B**47**, 6069 (1993); B.P. Stojković and D. Pines, Phys. Rev. B**55**, 8576 (1997).

³¹ A. Abanov, A.V. Chubukov, and J. Schmalian, cond-mat/0107421, to be published, Adv. Phys.

³² A.V. Chubukov, D. Pines, and J. Schmalian, cond-mat/0201140.

³³ J.A. Hertz, Phys. Rev. B**14**, 1165 (1976).

³⁴ A.J. Millis, Phys. Rev. B**48**, 7183 (1993).

³⁵ R.S. Markiewicz, presented at the "Workshop on Intrinsic Multiscale Structure and Dynamics in Complex Electronic Oxides", at the International Center for Theoretical Physics, Trieste, Italy, July 1-4, 2002.

³⁶ N. D. Mermin and H. Wagner, Phys. Rev. Lett. **17**, 1133 (1966).

³⁷ M. Ichioka and K. Machida, J. Phys. Soc. Jpn. **68**, 4020 (1999).

³⁸ B. Valenzuela, M.A.H. Vozmediano, and F. Guinea, Phys. Rev. B**62**, 11312 (2000).

³⁹ C. Kusko and R.S. Markiewicz, Phys. Rev. B**65**, 041102 (2002).

⁴⁰ C. Kusko, unpublished.

⁴¹ S. Onoda and M. Imada, J. Phys. Soc. Jpn. **68**, 2762 (1999).

⁴² N.M.R. Peres and M.A.N. Araújo, cond-mat/0303409, to be published, Phys. Stat. Sol.

⁴³ H.M. Rønnow, D.F. McMorrow, R. Coldea, A. Harrison, I.D. Youngson, T.G. Perring, G. Aeppli, O. Syljuåsen, K. Lefmann, and C. Rischel, Phys. Rev. Lett. **87**, 37202 (2001).

⁴⁴ P. Fulde, "Electron Correlations in Molecules and Solids", p. 305 (2d Ed.) (Springer, Berlin, 1993).

⁴⁵ N. Nagaosa, "Quantum Field Theory in Strongly Correlated Electronic Systems", (Springer, Berlin, 1999), Ch. 3.

⁴⁶ J. Kanamori, Prog. Theor. Phys. **30**, 275 (1963).

⁴⁷ P. Bénard, L. Chen, and A.-M.S. Tremblay, Phys. Rev. B**47**, 15217 (1993).

⁴⁸ Q. Si, Y. Zha, K. Levin, and J. Lu, Phys. Rev. B**47**, 9055 (1993).

⁴⁹ M. Lavagna and G. Stemman, Phys. Rev. B**49**, 4235 (1994).

⁵⁰ F. Onufrieva, P. Pfeuty, and M. Kiselev, Phys. Rev. Lett. **82**, 2370 (1999); F. Onufrieva and P. Pfeuty, Phys. Rev. B**61**, 799 (2000).

⁵¹ N. Harima, J. Matsuno, A. Fujimori, Y. Onose, Y. Taguchi, and Y. Tokura, Phys. Rev. B**64**, 217001 (2001).

⁵² N. Ichikawa, S. Uchida, J.M. Tranquada, T. Niemöller, P.M. Gehring, S.-H. Lee, and J.R. Schneider, Phys. Rev. Lett. **85**, 1738 (2000).

⁵³ V.M. Krasnov, Phys. Rev. B**65**, 140504 (2002).

⁵⁴ R.S. Markiewicz, Physica C**217**, 381 (1993).

⁵⁵ P. Bourges, L.P. Regnault, J.Y. Henry, C. Vettier, Y. Sidis, and P. Burlet, Physica B**215**, 30 (1995).

⁵⁶ J.V. Alvarez, J. González, F. Guinea, and M.A.H. Vozmediano, cond-mat/9804153.

⁵⁷ S. Sachdev, A.V. Chubukov, and A. Sokol, Phys. Rev. B**51**, 14874 (1995).

⁵⁸ S. Chakravarty, B.I. Halperin, and D.R. Nelson, Phys. Rev. Lett. **60**, 1057 (1988).

⁵⁹ P. Kopietz and S. Chakravarty, Phys. Rev. B**40**, 4858 (1989).

⁶⁰ M. Takahashi, Phys. Rev. B**40**, 2494 (1989).

⁶¹ N. Bulut, D.J. Scalapino, and S.R. White, Phys. Rev. B**47**, 2742 (1993).

⁶² J. Schmalian, D. Pines, and B. Stojković, Phys. Rev. B**60**, 667 (1999).

⁶³ C. Kim, F. Ronning, A. Damascelli, D.L. Feng, Z.-X. Shen, B.O. Wells, Y.J. Kim, R.J. Birgeneau, M.A. Kastner, L.L. Miller, H. Eisaki, and S. Uchida, Phys. Rev. B**65**, 174516 (2002).

⁶⁴ R. Hlubina and T.M. Rice, Phys. Rev. B**51**, 9253 (1995); N.P. Armitage, *et al.*, Phys. Rev. Lett. **87**, 147003 (2001).

⁶⁵ C. Pinettes and C. Lacroix, J. Phys. Cond. Matt. **6**, 10093 (1994).

⁶⁶ H.Q. Ding, Phys. Rev. Lett. **68**, 1927 (1992).

⁶⁷ A. Singh and Z. Tešanović, Phys. Rev. B**43**, 11445 (1991).

⁶⁸ B. Keimer, A. Aharonov, A. Auerbach, R.J. Birgeneau, A. Cassanho, Y. Endoh, R.W. Erwin, M.A. Kastner, and G. Shirane, Phys. Rev. B**45**, 7430 (1992).

⁶⁹ A.A. Katanin and A.P. Kampf, cond-mat/0111533.

⁷⁰ A. Singh, Z. Tešanović, H. Tang, G. Xiao, C.L. Chien, and J.C. Walker, Phys. Rev. Lett. **64**, 2571 (1990).

⁷¹ R.J. Birgeneau, H.J. Guggenheim, and G. Shirane, Phys. Rev. B**1**, 2211 (1970).

⁷² P. Anderson, Bull. A.P.S. **48**, 535 (2003).

⁷³ R.S. Markiewicz, Phys. Rev. Lett. **89**, 229703 (2002).

⁷⁴ T.D. Stanescu and P. Phillips, cond-mat/0301254.

⁷⁵ N. Miyakawa, P. Guptasarma, J.F. Zasadzinski, D.G. Hinks, and K.E. Gray, Phys. Rev. Lett. **80**, 157 (1998).

⁷⁶ V.M. Krasnov, Phys. Rev. B**65**, 140504 (2002).

⁷⁷ A. Yurgens, D. Winkler, T. Claeson, S. Ono, and Y. Ando, cond-mat/0212562.

⁷⁸ R.S. Markiewicz, J. Phys. Chem. Sol. **58**, 1179 (1997).

⁷⁹ G.V.M. Williams, J.L. Tallon, R. Michalak, and R. Dupree, Phys. Rev. B**57**, 8696 (1998).

⁸⁰ G. Esirgen, H.-B. Schüttler, C. Gröber, and H.G. Evertz, cond-mat/0105514.

⁸¹ L. Chen, C. Bourbonnais, T. Li, and A.-M.S. Tremblay, Phys. Rev. Lett. **66**, 369 (1991).

⁸² T.K. Lee, C.-M. Ho, and N. Nagaosa, Phys. Rev. Lett. **90**, 067001 (2003).

⁸³ F.C. Zhang and T.M. Rice, Phys. Rev. B**37**, 3759 (1988).

⁸⁴ M.S. Hybertsen, M. Schlüter, and N.E. Christensen, Phys. Rev. B**39**, 9028 (1989).

⁸⁵ S. Moukouri, S. Allen, F. Lemay, B. Kyung, D. Poulin, Y.M. Vilk, and A.-M.S. Tremblay, Phys. Rev. B**61**, 7887

(2000).

⁸⁶ I.S. Gradshteyn and I.M. Ryzhik, *Table of Integrals, Series, and Products*, 6th Ed. (Academic Press, San Diego, 2000), p. 883.

⁸⁷ F. Guinea, R.S. Markiewicz, and M.A.H. Vozmediano, cond-mat/0206208.

⁸⁸ O.K. Andersen, A.I. Liechtenstein, O. Jepsen, and F. Paulsen, *J. Phys. Chem. Solids* **56**, 1573 (1995).

⁸⁹ S. Chakravarty, A. Sudbo, P.W. Anderson, and S. Strong, *Science* **261**, 337 (1993).

⁹⁰ D.L. Feng, N.P. Armitage, D.H. Lu, A. Damascelli, J.P. Hu, P. Bogdanov, A. Lanzara, F. Ronning, K.M. Shen, H. Eisaki, C. Kim, Z.-X. Shen, J.-i. Shimoyama, and K. Kishio, *Phys. Rev. Lett.* **86**, 5550 (2001); Y.-D. Chuang, A.D. Gromko, A. Fedorov, Y. Aiura, K. Oka, Y. Ando, H. Eisaki, S.I. Uchida, and D.S. Dessau, *Phys. Rev. Lett.* **87**, 117002 (2001).

⁹¹ P.V. Bogdanov, A. Lanzara, X.J. Zhou, W.L. Yang, H. Eisaki, Z. Hussain, and Z.X. Shen, *Phys. Rev. Lett.* **89**, 167002 (2002).